

Semi-coupling of a Field-scale Resolving Land-surface Model and WRF-LES to Investigate the Influence of Land-surface Heterogeneity on Cloud Development

Jason Scot Simon¹, Andrew D. Bragg¹, Paul A Dirmeyer², and Nathaniel W. Chaney¹

¹Duke University

²George Mason University

November 30, 2022

Abstract

Contemporary Earth system models mostly ignore the sub-grid scale (SGS) heterogeneous coupling between the land surface and atmosphere, to a detriment that remains largely unknown. To both evaluate the effect of SGS heterogeneity for realistic scenarios and aid in the development of coupled land and atmosphere SGS parameterizations for global models, we present a study of the effect of sub-100 km scale land-surface heterogeneity on cloud development. In the primary experiment we use the Weather Research and Forecasting (WRF) model to conduct two large-eddy simulations over the Southern Great Plains (SGP) site using 100-m horizontal resolution on a domain that spans 100 km in each lateral direction. The first simulation uses high-resolution land-surface fields specified by an offline land-surface model (LSM), while the second uses homogenized land-surface fields found by taking a domain-averaged value of each field at each timestep. The atmospheric development of the heterogeneous and homogeneous simulations are compared, primarily in terms of cloud production and turbulent kinetic energy. It is seen that the heterogeneous case develops a mesoscale circulation pattern which generates additional clouds and turbulence compared to the homogeneous case. Additional experiments isolate sources of heterogeneity in the LSM (including forcing meteorology) to better understand relevant land-surface processes, and modify the Bowen ratio and initial wind profile of the heterogeneous case to clarify the results seen. Finally two additional days at the SGP site are simulated confirming the increase in cloud production in heterogeneous cases.

1 **Semi-coupling of a Field-scale Resolving Land-surface**
2 **Model and WRF-LES to Investigate the Influence of**
3 **Land-surface Heterogeneity on Cloud Development**

4 **Jason S. Simon¹, Andrew D. Bragg¹, Paul A. Dirmeyer², and Nathaniel W.**
5 **Chaney¹**

6 ¹Duke University
7 ²George Mason University

8 **Key Points:**

- 9 • Large-eddy simulation is used to study fine-scale heterogeneity in land-atmosphere
10 coupling
11 • Spatial patterns of dry and wet areas increase cloud production via mesoscale cir-
12 culations
13 • Sub-grid scale heterogeneity should ideally be included in global model parame-
14 terizations

Abstract

Contemporary Earth system models mostly ignore the sub-grid scale (SGS) heterogeneous coupling between the land surface and atmosphere, to a detriment that remains largely unknown. To both evaluate the effect of SGS heterogeneity for realistic scenarios and aid in the development of coupled land and atmosphere SGS parameterizations for global models, we present a study of the effect of sub-100 km scale land-surface heterogeneity on cloud development. In the primary experiment we use the Weather Research and Forecasting (WRF) model to conduct two large-eddy simulations over the Southern Great Plains (SGP) site using 100-m horizontal resolution on a domain that spans 100 km in each lateral direction. The first simulation uses high-resolution land-surface fields specified by an offline land-surface model (LSM), while the second uses homogenized land-surface fields found by taking a domain-averaged value of each field at each timestep. The atmospheric development of the heterogeneous and homogeneous simulations are compared, primarily in terms of cloud production and turbulent kinetic energy. It is seen that the heterogeneous case develops a mesoscale circulation pattern which generates additional clouds and turbulence compared to the homogeneous case. Additional experiments isolate sources of heterogeneity in the LSM (including forcing meteorology) to better understand relevant land-surface processes, and modify the Bowen ratio and initial wind profile of the heterogeneous case to clarify the results seen. Finally two additional days at the SGP site are simulated confirming the increase in cloud production in heterogeneous cases.

Plain Language Summary

A modern Earth system model combines an atmospheric model and land-surface model, and the two interact during a simulation. Due to computational constraints, global models today use grids where very large areas (sometimes in excess of 10,000 square kilometers) are represented by a single point, making it impossible to directly represent many important features, particularly those related to the development of clouds and rain. Approximations of these processes that cannot be represented are included by simpler sub-models called parameterizations, which often base calculations on average values over the area they are modeling. To aid in the improvement of these parameterizations, a high-resolution model (where each point represents only 0.01 square kilometers) is used to simulate three summer days in Oklahoma over a total area of 10,000 square kilometers. It is seen that simulations where the land surface has moist and dry patches from previous rain events produce more clouds than simulations where the same amount of soil moisture is evenly distributed over the entire surface. We hope that this and future work will both motivate and aid efforts to add considerations for the spatial distribution of features, in addition to their average, to the parameterizations used in Earth system models.

1 Introduction

A critical challenge in characterizing land-atmosphere interactions across scales in Earth system models (ESMs) is the non-linearity that emerges as a result of spatial heterogeneities over land (e.g., land use and topography) (Albertson et al., 2001; Bou-Zeid et al., 2004; Huang & Margulis, 2013; Shao et al., 2013; Clark et al., 2015). These complex interactions between the land-surface processes and the underlying physical environment drive the spatial complexity of surface fluxes and states (Western et al., 1999; Gómez-Plaza et al., 2001; Jacobs et al., 2004; Chaney et al., 2015). As a result, the macroscale behavior of the water and energy cycles cannot be disentangled from their fine-scale processes and interactions. The heterogeneities that emerge over land, in turn, can play a key role in many important atmospheric processes, such as setting the atmospheric boundary layer (ABL) depth, initiating convection, and spawning mesoscale circulations (Ntelekos

et al., 2008; Kustas & Albertson, 2003; Timmermans et al., 2008; Bertoldi et al., 2013; Gutowski et al., 2020). Although progress is being made in understanding the role of multi-scale land heterogeneity on microscale and mesoscale meteorological processes in regional and local studies (Kustas & Albertson, 2003; Talbot et al., 2012; Bertoldi et al., 2013; Huang & Margulis, 2013; Shrestha et al., 2014; Senatore et al., 2015), its role in land-atmosphere interactions in the climate system as a whole remains mostly unknown. This is primarily due to the over-simplistic coupling between existing sub-grid parameterizations in land surface models and atmospheric models (e.g., tiling schemes, Ducharne et al., 2000; Bonan et al., 2002; Milly et al., 2014; Chaney et al., 2018; Lawrence et al., 2019). Existing ESMs only exchange sub-grid spatial mean fluxes of mass and energy between the land and atmosphere while disregarding higher order sub-grid spatial statistics (e.g., spatial variance). Convection and turbulence parameterizations in atmospheric circulation models are moving towards the inclusion of higher-order SGS processes (e.g., Cloud Layers Unified By Binormals (CLUBB) and Eddy Diffusivity Mass Flux (EDMF), Golaz et al., 2002; Sušelj et al., 2013), providing an opportunity for potential coupling with the SGS heterogeneity of the land surface.

There have been many modeling studies on heterogeneous land surfaces and their effects on atmospheric dynamics, primarily using idealized surface flux fields and initial atmospheres. Pielke Sr (2001) gives a very thorough theoretical background and review of work done studying the effect of heterogeneous spatial distributions of sensible and latent heat fluxes from the land surface on the development of cumulus convective rainfall in the atmosphere. Notably, Avissar and Schmidt (1998) studied the influence of heterogeneity in the surface sensible heat flux field in a dry atmosphere using a large-eddy simulation (LES), finding that the scale of the surface heat flux does influence the development of the atmospheric boundary layer (ABL) in the absence of a mean wind, but that the effects of the surface heterogeneity are “virtually eliminated” by a background wind of 5 m s^{-1} . They also found that the presence of moisture combined with heterogeneous fluxes could lead to pockets of moisture which may lead to cloud development which would not be present in a homogeneous case. They finally concluded that for heterogeneity of scales smaller than $5 - 10 \text{ km}$, a mean flux value over a grid cell may be used without affecting the CBL development, even with no background wind present. A modeling study by Findell and Eltahir (2003), using a nested mesoscale framework with uniform surface moisture, found that the influence of the background wind on surface fluxes, as it relates to triggering convection, is more nuanced, and can either suppress or enhance convection depending on the direction and amount of shear. More recently, Kang (2016) conducted an LES study of scales of surface-flux heterogeneity, finding that surface-flux fields with large Bowen ratios and large scales of heterogeneity are able to trigger deep convection, where more homogeneous cases are not. Kang (2020) conducted a similar LES study with multiple degrees of heterogeneity in the surface-flux fields finding that heterogeneous surface fields reduced the decay of turbulent kinetic energy (TKE) in the atmosphere.

Heterogeneous surface fields have also been studied observationally, often with noted differences from modeling studies. Taylor et al. (2011) used satellite observations to study the influence of soil moisture on the development of convective rain storms in West Africa, concluding that soil moisture variations at $\mathcal{O}(10 - 40 \text{ km})$ strongly control storm development in the region. Taylor et al. (2012) studied the feedback mechanisms between soil moisture and convective storms from global observations, finding that drier soils are more likely to produce afternoon rainfall events while wetter soils show no preference for rain development. They note that this result is in contrast to many weather and climate models, which show a preference for rainfall development over wetter soils. Phillips and Klein (2014) studied the Southern Great Plains (SGP) site and found that, while large-scale forcings tend to dominate, there are some cases where local feedbacks from the surface play a role in the atmosphere, particularly as soil dries after a precipitation event. They

118 also note a contrast between their results and modeling efforts, where models tend to
 119 over-predict a coupling between soil moisture and precipitation.

120 To aid in the development of an effective sub-grid coupling between the modeled
 121 land-surface and atmospheric heterogeneity in ESMs, more must be known about the
 122 impact of land-surface heterogeneity on atmospheric dynamics. To this end, the study
 123 presented here uses output from HydroBlocks, a field-scale resolving land-surface model
 124 (LSM), to drive the surface of the Weather Research and Forecasting (WRF) model, run
 125 in LES mode, over the SGP site using initial profiles and large-scale temperature and
 126 moisture fluxes based on observations. The result is a realistic study on the coupling be-
 127 tween the land surface and ABL development over a diurnal cycle, with a specific inter-
 128 est in the role of land-surface heterogeneity on cloud production. A domain area of 100
 129 km \times 100 km is used, which allows domain-wide mean values to be taken as a represen-
 130 tation of a grid-scale value in a global model and the effects of land-surface heterogene-
 131 ity, which would be SGS on a climate-scale grid, on the grid-scale signal to be studied
 132 directly via LES. With this study, we aim to help to answer three questions which are
 133 key to the development of global-scale parameterizations which consider SGS heterogene-
 134 ity. First, are the effects of land-surface heterogeneity which are seen in more idealized
 135 LES studies, specifically emergent mesoscale circulations between wet and dry areas, ob-
 136 served when using realistic surface flux fields? Second, what is the impact on the macroscale
 137 (domain-wide) signal of the heterogeneous land surfaces? Finally, what is the relative
 138 impact of the different sources of heterogeneity in the LSM (e.g., soil type, rivers and
 139 surface water, soil moisture, etc.)?

140 The primary experiment here is a pair of simulations of September 24, 2017: the
 141 first simulation uses the high-resolution HydroBlocks land surface while the second spa-
 142 tially homogenizes the land surface by using domain-averaged values at each grid point
 143 (Sec. 3.1). Cases are then considered where only certain land-surface features are rep-
 144 resented heterogeneously in the driving HydroBlocks simulation, generating different scales
 145 of surface heterogeneity (Sec. 3.2). Additional cases are also considered by modifying the
 146 heterogeneous case so that the Bowen ratio at the surface is increased, and the initial
 147 wind profile is adjusted (Sec. 3.3). Finally, the primary heterogeneous vs. homogeneous
 148 experiment is repeated for simulations of June 10, 2016 and July 16, 2017 and are an-
 149 alyzed briefly (Sec. 3.4).

150 2 Model description

151 2.1 WRF

152 Atmospheric simulations are conducted using version 3.8.1 of the WRF model (Skamarock
 153 et al., 2008) as an LES (WRF-LES). Model settings largely follow those used in the LES
 154 ARM Symbiotic Simulation and Observation Workflow (LASSO) campaign (W. Gustafson
 155 et al., 2019; W. I. Gustafson et al., 2020), which is publicly-available dataset of LES cases
 156 over the SGP site. The key difference between the LASSO simulations and those pre-
 157 sented here is the specification of heterogeneous surface conditions. The LASSO simu-
 158 lations use spatially-uniform, time-evolving surface fields for sensible heat flux, latent
 159 heat flux, and skin temperature (specified directly), as well as a spatially-uniform and
 160 constant momentum roughness. Here, heterogeneous cases use two-dimensional, time-
 161 evolving surface fields for sensible heat flux, latent heat flux, skin temperature (found
 162 via specified emissivity and upward longwave radiation fields), albedo, and momentum
 163 roughness, all obtained from the HydroBlocks LSM described in Sec. 2.2. The surface
 164 fields from the HydroBlocks LSM are semi-coupled to the atmosphere in the WRF model,
 165 i.e., the LSM is run offline using reanalysis meteorology, and there is no feedback from
 166 the atmosphere to the land surface in the LES. Other notable differences between the
 167 WRF settings used here and those used by LASSO are the expansion of the domain to
 168 100 km \times 100 km (where the LASSO domain is 25 km \times 25 km), the use of the isotropic

three-dimensional Smagorinsky-Lilly turbulence closure model (where LASSO uses the isotropic three-dimensional Deardorff model), and the inclusion of a Coriolis forcing (where LASSO considers every grid point to be at the same latitude and longitude).

Following the LASSO configuration, simulations use the Thompson graupel microphysics scheme and the RRTMG radiation scheme (though surfaces are specified offline by HydroBlocks) with the cumulus and PBL schemes turned off. The horizontal resolution is $\Delta_{x,y} = 100$ m with a timestep of 0.5 s. The domain is approximately 14.5 km tall with 227 vertical levels and a vertical resolution of $\Delta_z = 30$ m in the lower 5 km of the column. Periodic boundary conditions are used in both lateral directions and a w -Rayleigh damping layer is applied in the upper 2 km of the column. The LES domain uses a flat bottom boundary, though terrain is considered by the offline HydroBlocks simulation for surface routing. Initial profiles for potential temperature, water vapor mixing ratio, and lateral velocity components are obtained from the LASSO database and are applied uniformly to the domain. A relatively unique feature of the LASSO simulations is the inclusion of large-scale heat and moisture flux profiles that are applied uniformly on every column in the grid at each timestep, allowing the use of a single non-nested domain while still providing considerations for large-scale meteorology. Forcing data for these large-scale fluxes are also obtained from the LASSO database.

2.2 HydroBlocks

HydroBlocks is a field-scale resolving land-surface model (Chaney, Metcalfe, & Wood, 2016) that accounts for the water, energy, and carbon balance to solve land-surface processes at high spatial and temporal resolutions. HydroBlocks leverages the repeating patterns that exist over the landscape (i.e., the spatial organization) by clustering areas of assumed similar hydrologic behaviour into hydrologic response units (HRUs). The simulation of these HRUs and their spatial interactions allows the modeling of the water and energy cycles at field scales (30 m) over regional to continental extents (Chaney, Metcalfe, & Wood, 2016; Chaney et al., 2020; Vergopolan et al., 2020). The core of HydroBlocks is the Noah-MP vertical land surface scheme (Niu et al., 2011). HydroBlocks applies Noah-MP in an HRU framework to explicitly represent the spatial heterogeneity of surface processes down to field scale. At each timestep, the land-surface scheme updates the hydrological states at each HRU; and the HRUs dynamically interact laterally via subsurface flow.

For this study, HydroBlocks is spun up for two years and uses high-resolution (30 m) soil type and land cover maps from the Probabilistic Remapping of SSURGO (POLARIS) (Chaney, Wood, et al., 2016; Chaney et al., 2019) and National Land Cover Database (NLCD) (Homer et al., 2012) datasets, respectively, and one-eighth degree NLDAS-2 meteorology (Cosgrove et al., 2003; Mitchell et al., 2004) with NCEP Stage-IV radar rainfall (~ 4 km) data (Lin & Mitchell, 2005). The hourly state of the land surface produced by HydroBlocks for the period of interest is then used to specify surface values in the WRF model for: sensible heat flux, latent heat flux, momentum roughness coefficient, albedo, emissivity, and upward longwave radiation. Surface skin temperature is then diagnosed from emissivity and upward longwave radiation, and homogenized skin temperature is similarly diagnosed from homogenized upward longwave radiation and homogenized emissivity (rather than a domain-average of skin temperature directly). For consistency, surface-flux fields are adjusted so that the domain-wide averages match the time-evolving scalar surface fluxes specified by the LASSO campaign, which are from the observationally-improved VARANAL dataset.

3 Results

Simulations are performed on a 100 km \times 100 km domain over the SGP site, centered at 36.6° N, 97.5° W. The domain is largely cultivated cropland and grassland, with

219 a few small urban areas and a tributary of the Arkansas River running primarily west-
 220 east through the domain (Fig. 1). The basic heterogeneous and homogeneous cases are
 221 the primary experiment, and the additional experiments are used to clarify the results
 222 seen in the primary experiment. Comparisons between cases are made primarily by eval-
 223 uating the differences in the development of liquid water path (LWP) in time and space.
 224 LWP is of key interest because it serves as a proxy for cloud production and has a high
 225 relevance to radiation (Sengupta et al., 2003). In the following discussion, x , y and z re-
 226 fer to the grid’s west-east, south-north and vertical directions, respectively, and u , v and
 227 w refer to their respective velocity components.



Figure 1. Map of the simulation domain, centered at the SGP site.

3.1 Heterogeneous vs. homogeneous

228

229 The primary day considered is September 24, 2017. This day was chosen due to
 230 the appreciable spatial heterogeneity in the LSM simulations. Following the LASSO setup,
 231 simulations are run for 15 hours beginning at 0538 LST (1200 UTC). Over the $100 \text{ km} \times 100 \text{ km}$
 232 domain, for both the heterogeneous and homogeneous simulations, the average sensible heat flux peaks at $t \approx 1030 \text{ LST}$ with a magnitude of approximately 215 W m^{-2} ,
 233 and the domain-averaged latent heat flux peaks at the same time with a magnitude of
 234 approximately 130 W m^{-2} (Fig. 2a). In the heterogeneous case the standard deviations
 235 of the sensible and latent heat fluxes both peak at $t \approx 1230 \text{ LST}$ with values of approx-
 236 imately 40 and 45 W m^{-2} , respectively (Fig. 2b). Both simulations are initialized with
 237 the same domain-wide profiles for potential temperature, water vapor mixing ratio and
 238 lateral velocity components, shown in Fig. 3. The initial profile is stable with a water
 239 vapor mixing ratio of $\mathcal{O}(10 \text{ g kg}^{-1})$ in the lower 4 km and a wind profile which is pre-
 240 dominantly south-north with $v \approx 15 \text{ m s}^{-1}$ in the lower 10 km of the column.
 241

242 Maps of the surface sensible heat flux and latent heat flux used to drive the WRF-
 243 LES surface, upscaled to $\Delta_{x,y} = 100 \text{ m}$ from the HydroBlocks output, are shown in Fig. 4
 244 at $t = 1238 \text{ LST}$, corresponding to the peak standard deviations for sensible and la-
 245 tent heat fluxes in the diurnal cycle. This day was chosen for the large moist patch in

246 the east of the domain, which is a result of scattered thunderstorms that occurred a few
 247 days before. Surface fields in the LES are specified from HydroBlocks every hour on the
 248 hour and are linearly interpolated in time at each timestep in between. The homogeneous
 249 case specifies the domain-averaged value of the aforementioned surface fields at each grid
 250 point, calculated at each timestep.

251 The heterogeneous and homogeneous simulations show a notable difference in both
 252 domain-wide LWP (Fig. 5a) and vertically-integrated, mass-coupled TKE (Fig. 5b) in
 253 time. Both cases begin to produce liquid water in the atmosphere at $t \approx 0930$ LST, but
 254 the two cases diverge at $t \approx 1130$ LST. The heterogeneous case continues to produce
 255 liquid water more rapidly, reaching a peak of nearly 300 g m^{-2} just before $t = 1400$ LST,
 256 while the homogeneous case has a lower rate of production, reaching a peak of $\sim 250 \text{ g m}^{-2}$
 257 also near 1400 LST. Production of TKE between the two cases shows even larger dif-
 258 ferences, where the two cases diverge again at $t \approx 1130$ LST with the heterogeneous
 259 case reaching a much larger peak value than the homogeneous case.

260 To examine differences in spatial liquid water production, a map of each grid point's
 261 maximum LWP value throughout the duration of the simulation is shown for the het-
 262 erogeneous (Fig. 6a) and homogeneous (Fig. 6b) cases. The heterogeneous case shows
 263 a very strong pattern of high liquid water production in the western half of the domain
 264 and low liquid water production in the eastern half of the domain, while the homoge-
 265 neous case is more distributed throughout the center of the domain. Recalling that this
 266 case has a large moist patch in the east of the domain and a predominantly south-north
 267 flow, it appears that liquid water production for this case has a preference for areas with
 268 a high sensible heat flux at the surface, rather than areas with a high latent heat flux.
 269 We will see in Sec. 3.3 that the larger sensible heat fluxes alone are not sufficient to gen-
 270 erate the levels of cloud production seen in the heterogeneous case, indicating that some
 271 circulation pattern potentially exists between the moist and dry areas of the domain; a
 272 phenomenon that has been observed in idealized modeling studies (e.g., Han et al., 2019).

273 Emergent mesoscale circulations in the heterogeneous case are examined with cross-
 274 section profiles of $u(x)$ at $t = 1408$ LST, approximately corresponding to the time of
 275 peak LWP in the domain, at $y = 45$ km (Fig. 7a) and averaged over the full domain
 276 in the y direction (Fig. 7b). The profiles reveal the anticipated general circulation be-
 277 havior, where flow is primarily westward in the lower 2 km of the domain with a coher-
 278 ent band of eastward flow aloft which reaches a height of $z \approx 5$ km at $x \approx 35$ km, grad-
 279 ually descending to $z \approx 3$ km over the eastern edge of the domain. Due to the periodic
 280 lateral boundary conditions, the lower end of this layer from the eastern edge is also present
 281 in the westernmost 20 km of the domain. Up- and downdrafts are largely averaged out
 282 in the y -averaged cross-section, but are much more visible in the $y = 45$ km cross-section
 283 where a large visible updraft forms at $x \approx 35$ km, directly beneath the high point of
 284 the band of eastward flow aloft.

285 The same cross-sections of u are shown for the homogeneous case in (Fig. 8). The
 286 $y = 45$ km cross-section for the homogeneous case (Fig. 8a) does show many clear up-
 287 welling events, but they appear to dissipate in a few kilometers without developing any
 288 coherent circulation pattern, as is expected of an atmosphere with a uniform surface heat-
 289 ing. The y -averaged cross-section for the homogeneous case (Fig. 8b) does have a band
 290 of eastward flow at $z \approx 4$ km, but its magnitude is much lower than in the heteroge-
 291 neous case, and much of the flow appears closer to stagnant. There is also a strong west-
 292 ward flow in the lower 2 km of the homogeneous case, but without any clear pattern of
 293 upwelling anywhere in the domain. Unlike in the heterogeneous case, both bands in the
 294 homogeneous case span the full length of the domain in x .

295 Similar cross-section profiles across x of relative humidity and cloud mixing ratio
 296 domain-averaged in y , shown for the heterogeneous case in Figs. 7c, d and the homoge-
 297 neous case at in Figs. 8c, d, respectively, further inform on the differences between the

two simulations, largely confirming what is already seen. The heterogeneous case has a very non-uniform profile of relative humidity in the x cross-section with well-mixed values reaching $z \approx 5$ km in the westernmost ~ 40 km of the domain, which appear to also pass through the periodic lateral boundary into the easternmost ~ 10 km of the domain. In the center of the domain the relative humidity reaches a maximum height of $z \approx 4$ km. Cloud production in the heterogeneous case is similarly focused in the west of the domain reaching an average cloud top above $z = 6$ km, with some sparser and lower clouds in the east of the domain that appear to have advected across the boundary from the western edge of the domain. The homogeneous case, conversely and expectedly, shows a very uniform mixing of relative humidity with the well-mixed layer reaching a height $z \approx 5$ km everywhere in the x cross-section. Cloud production in the homogeneous case is also very uniform across the domain, producing very sparse clouds compared to the heterogeneous simulation with a cloud top also at $z \approx 5$ km.

Compared to the homogeneous case, liquid water production in the heterogeneous case appears to benefit from both the moist and dry patches in its surface forcing, despite them not being co-located, via the latent heat flux from the moist patch being transported laterally to drier areas with a higher sensible heat flux which then lifts the moist air past the lifted condensation level resulting in local cloud production. The homogeneous case, which has the same domain-wide total surface latent and sensible heat fluxes, is unable to generate the same cloud production without local areas of higher sensible heat flux to produce similar local updrafts for the moisture that is present in the boundary layer. The following sections will further investigate the mechanisms driving the behavior of the heterogeneous case seen here.

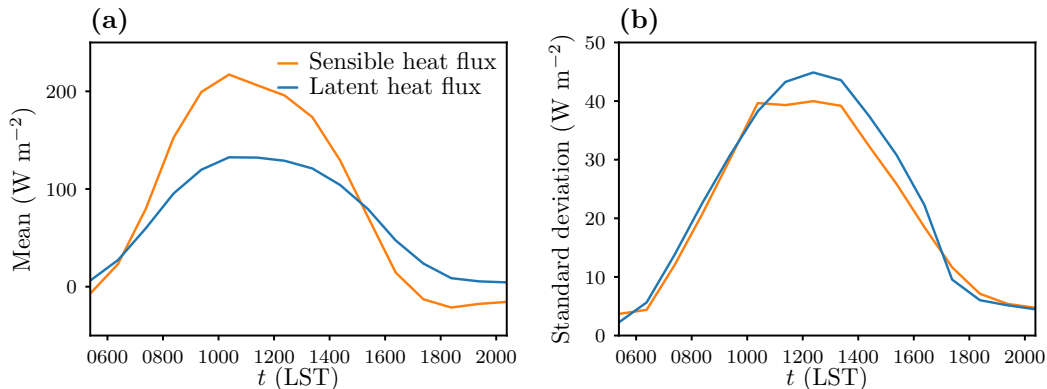


Figure 2. Time series of the surface sensible heat and latent heat fluxes used for the September 24, 2017 simulations: (a) domain mean for heterogeneous and homogeneous cases, (b) standard deviation for the heterogeneous case.

3.2 Land-surface components

The heterogeneity in the surface fields used in Sec. 3.1 is the result of four primary sources in the HydroBlocks model: river routing and subsurface flow, soil type, land cover, and forcing meteorology. To better understand the role of land-surface heterogeneity in atmospheric dynamics we present four additional WRF simulations which use surface maps from HydroBlocks when considering only certain sources of heterogeneity. The first simulation (the “R” case) contains surface heterogeneity generated only by rivers and subsurface flow, using surface fields from a HydroBlocks simulation which calculates river routing and subsurface flow as normal but uses homogenized fields for soil type, land cover, and forcing meteorology. The second simulation (“R+S”) follows the same methodol-

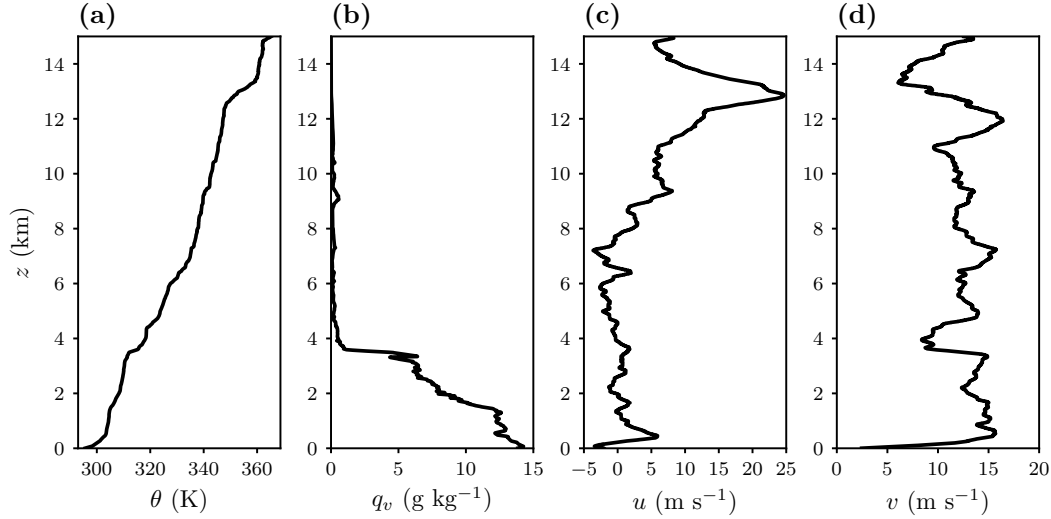


Figure 3. Initial profiles used for the September 24, 2017 simulations: (a) potential temperature, (b) water vapor mixing ratio, (c) u -velocity, (d) v -velocity.

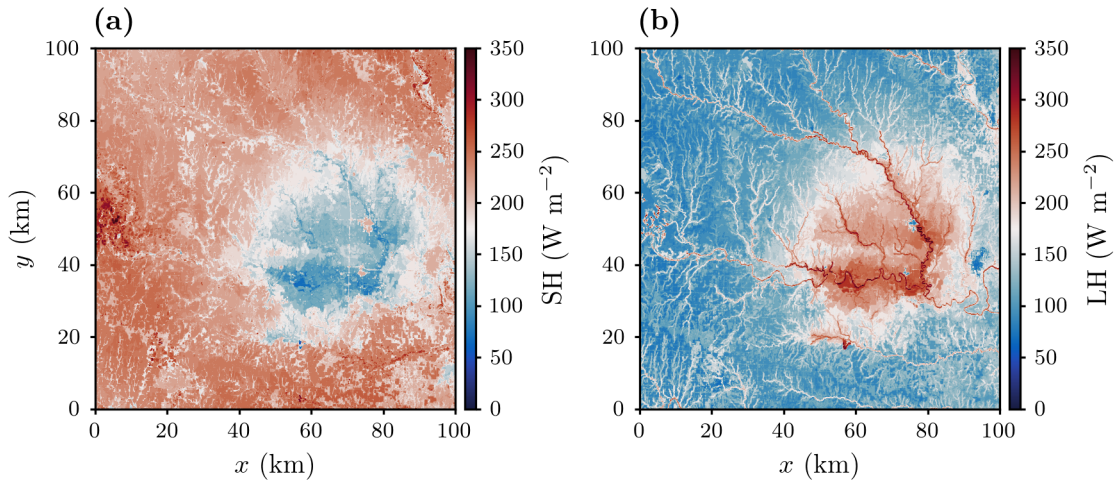


Figure 4. Heterogeneous surface values for the September 24, 2017 simulations at $t = 1238$ LST, upscaled from HydroBlocks: (a) sensible heat flux, (b) latent heat flux.

331
 332
 333
 334
 335
 336
 337
 338
 339
 340

ogy but the driving HydroBlocks simulation also uses the heterogeneous soil-type map. The third simulation (“R+S+LC”) uses the heterogeneous land cover field in addition to rivers/subsurface flow and soil type. The fourth simulation (“M”) isolates surface heterogeneity generated by the meteorology driving the LSM by homogenizing the other fields. Each case is energetically constrained so that the domain-averaged surface sensible and latent heat fluxes remain unchanged from the base cases, thus only the standard deviations and spatial scales of heterogeneity differ between these four cases and those in Sec. 3.1. The fully heterogeneous case from Sec. 3.1 is equivalent to an “R+S+LC+M” case and is used here, along with its corresponding fully homogeneous case, as a reference for comparison.

341
 342

Standard deviations of surface sensible heat flux and latent heat flux in time are shown in Fig. 9a, b, respectively. The sensible heat flux standard deviations are, very

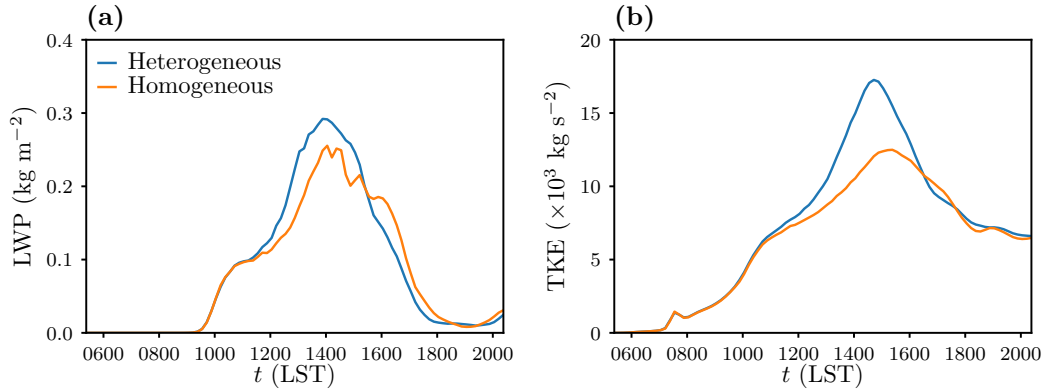


Figure 5. Domain-wide fields in time from the heterogeneous and homogeneous September 24, 2017 simulations: (a) LWP, (b) vertically integrated, mass-coupled TKE.

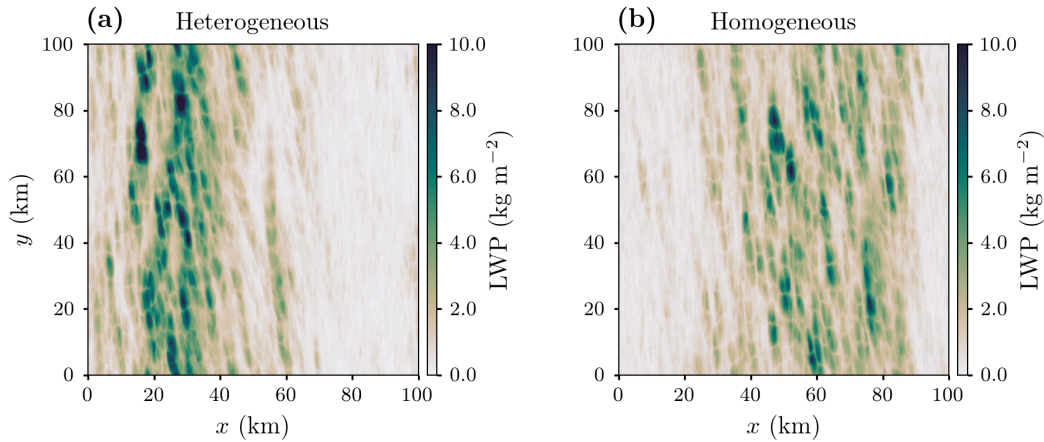


Figure 6. Maximum values of LWP at each grid point throughout the duration of the September 24, 2017 simulations using: (a) heterogeneous land surfaces, (b) homogeneous land surfaces.

343 approximately, linearly distributed with the R case peaking at the lowest value (approx-
 344 imately 10 W m^{-2}), followed by the R+S and R+S+LC cases. The M case has a peak
 345 standard deviation just below the fully heterogeneous case's peak value (approximately
 346 40 W m^{-2}). The latent heat flux standard deviations, on the other hand, have two clear
 347 groups: the R, R+S, and R+S+LC cases which have peak values from approximately
 348 10 to 20 W m^{-2} , and the fully heterogeneous and M cases which are nearly overlapping
 349 with a peak value of approximately 45 W m^{-2} .

350 Maps of surface sensible heat flux and latent heat flux at $t = 1238 \text{ LST}$ for the
 351 four cases are shown in Fig. 10. The R case has a largely homogeneous sensible heat flux
 352 field (Fig. 10a1) and a river network visible in the latent heat flux field (Fig. 10b1) which,
 353 despite appearing very heterogeneous, contains only small spatial scales of heterogene-
 354 ity and spans the entire domain. The R+S case has a small visual increase in sensible
 355 and latent heat flux heterogeneity compared to the R case (Fig. 10a2, b2, respectively).
 356 The R+S+LC case adds considerable visual detail to the sensible heat flux (Fig. 10a3)
 357 and latent heat flux (Fig. 10b3) fields compared to the R+S case. The M case is largely
 358 homogeneous in both fields (Fig. 10a4, b4) aside from the $\mathcal{O}(50 \text{ km})$ moist patch in the

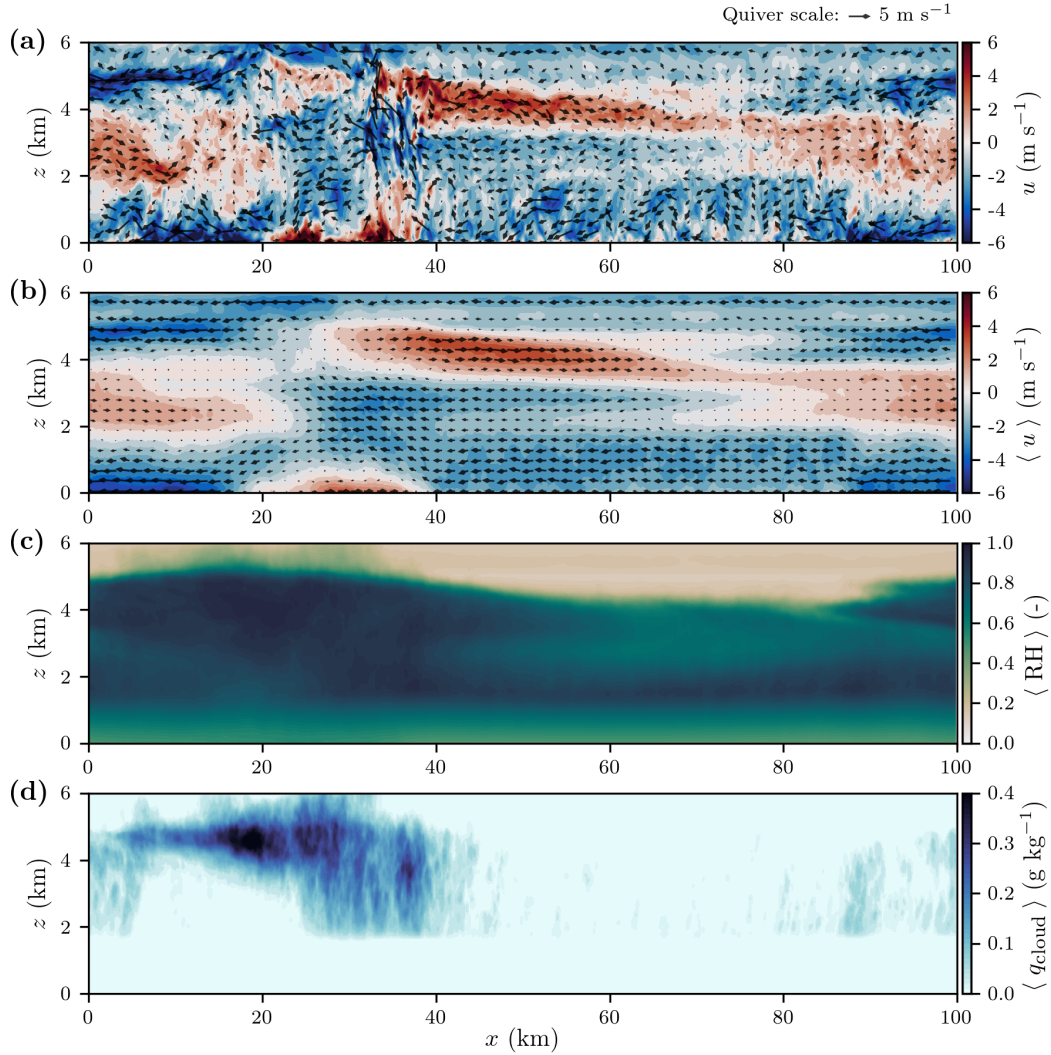


Figure 7. Profiles from the September 24, 2017 simulation using heterogeneous surfaces at $t = 1408$ LST of: (a) u -velocity along x at $y = 45$ km, (b) u -velocity along x and domain-averaged in y , (c) relative humidity along x and domain-averaged in y , (d) cloud mixing ratio along x and domain-averaged in y .

359 east of the domain, confirming that heterogeneous forcing meteorology is responsible for
 360 the larger scales of land-surface heterogeneity seen in the fully heterogeneous case.

361 Considering the resulting time series of LWP and TKE for these cases (Fig. 11a,
 362 b, respectively), the R and R+S cases are nearly indistinguishable from the fully homo-
 363 geneous case while the R+S+LC case follows the fully homogeneous case until $t \approx 1330$ LST
 364 but then has a larger peak than the homogeneous case for both LWP and TKE. The M
 365 case produces liquid water and TKE very similarly to the fully heterogeneous case, where
 366 both diverge from the other cases at $t \approx 1130$ LST with similar production rates. The
 367 M case produces a slightly larger peak in LWP than the fully heterogeneous case, while
 368 the TKE production is nearly identical between the two. The M case produces nearly
 369 all of its liquid water in the westernmost 40 km of the domain while the other three cases
 are relatively homogeneous (not shown).

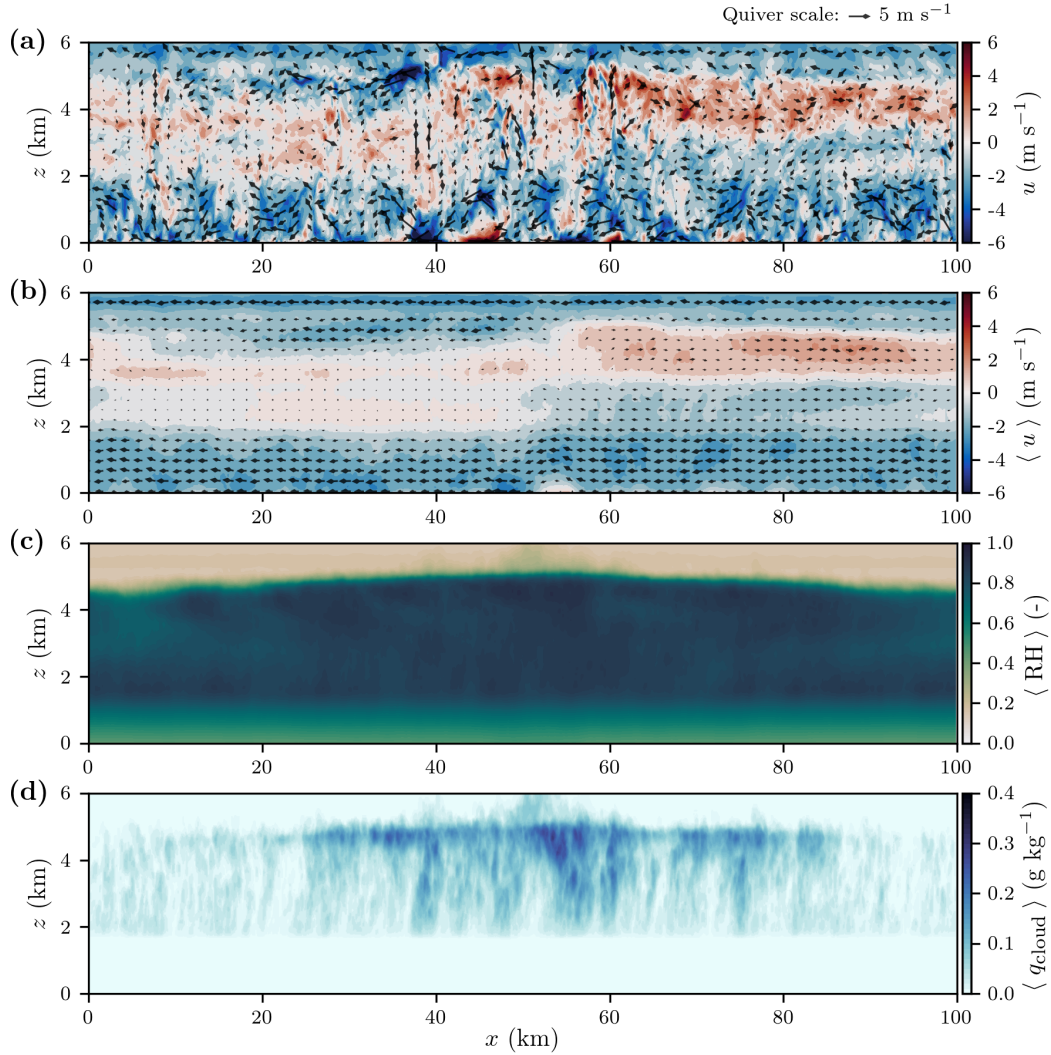


Figure 8. Profiles from the September 24, 2017 simulation using homogeneous surfaces at $t = 1408$ LST of: (a) u -velocity along x at $y = 45$ km, (b) u -velocity along x and domain-averaged in y , (c) relative humidity along x and domain-averaged in y , (d) cloud mixing ratio along x and domain-averaged in y .

371 It is seen that heterogeneous meteorology in the LSM is the primary driver of atmospherically-
 372 relevant heterogeneity in the land surface, even in the presence of a relatively strong wind
 373 profile as used here. While this seems trivial, land-surface heterogeneity is often tradi-
 374 tionally seen as unimportant in the presence of even moderate winds as it will be “blended
 375 out” in the atmospheric boundary layer. It is also seen that the standard deviation of
 376 surface heterogeneity alone is insufficient to describe its impact on atmospheric dynam-
 377 ics, as demonstrated by the close agreement in LWP and TKE production between the
 378 fully homogeneous, R, and R+S cases despite significant differences in standard devi-
 379 ations.

380 3.3 Modified Bowen ratio and wind profile cases

381 It is proposed in Sec. 3.1 that the difference observed in cloud production between
 382 the heterogeneous and homogeneous cases is generated by emergent circulations between

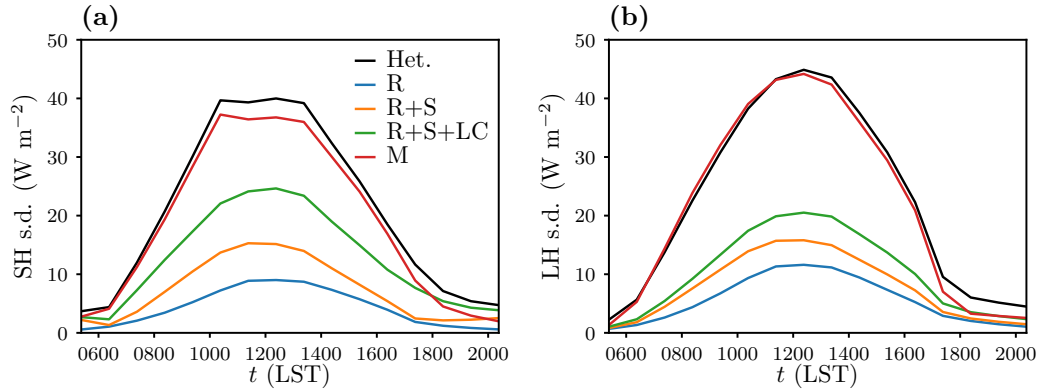


Figure 9. Time series of standard deviations of the surface fluxes used for the September 24, 2017 simulations where the land model includes heterogeneity from only rivers (R), rivers and soil type (R+S), rivers, soil type and land cover (R+S+LC), and only forcing meteorology (M): (a) sensible heat, (b) latent heat. The fully heterogeneous case is also shown for comparison.

383 the moist and dry areas of the land surface. However, it is also possible that the local
 384 areas of high sensible heat flux in the heterogeneous case are instead lifting the mois-
 385 ture that exists uniformly in the domain from the initial profile and large-scale forcing.
 386 To evaluate these two possible explanations, we consider heterogeneous cases with all
 387 of the surface latent heat flux at each grid point converted to additional sensible heat
 388 flux at the same grid point (the “0% latent heat” case) and 80% of the surface latent heat
 389 flux at each grid point converted to additional sensible heat flux at the same grid point
 390 (the “20% latent heat” case). Additionally, simulations in previous sections have all used
 391 the same initial wind profile, the consequence of which is unknown. To evaluate the ef-
 392 fect of the wind profile, we consider a case with no wind in the initial profile (the “no
 393 wind” case) and a case where the wind at each vertical level of the initial profile is re-
 394 oriented to be purely west-to-east (the “w-e wind” case). Both modified-wind cases use
 395 the unmodified heterogeneous land surface fields.

396 Time series of LWP and TKE for all four cases are shown in Fig. 12a, b, respec-
 397 tively. The increase in surface sensible heat flux in the 0% and 20% latent heat cases slightly
 398 speeds up the onset of liquid water production and significantly increases the TKE pro-
 399 duction in the first six hours compared to the fully heterogeneous and homogeneous cases.
 400 Both the 0% and 20% latent heat cases produce more liquid water in the first 8 hours
 401 of the simulation than the fully homogeneous case, but still less than the fully hetero-
 402 geneous case once the heterogeneous case begins its high rate of production at $t \approx 1130$ LST.
 403 As well, the peak LWP values of both the 0% and 20% latent heat cases are very simi-
 404 lar in magnitude to the fully homogeneous case. Both the 0% and 20% latent heat cases
 405 produce a large amount of TKE early but decline in their production rate after 1000 LST,
 406 and are thus ultimately surpassed by the fully heterogeneous case. Maps of maximum
 407 LWP throughout the simulation for the 0% and 20% latent heat cases show largely ho-
 408 mogeneous liquid water production (not shown).

409 The results from the 0% and 20% latent heat cases give confidence that the pres-
 410 ence of larger local sensible heat fluxes alone cannot explain the increase in liquid wa-
 411 ter production seen in the heterogeneous case compared to the homogeneous case. The
 412 results also imply that surface sensible heat flux drives the onset of TKE in the domain
 413 (for the same initial wind profile), which is also coupled to some degree to the initial liq-
 414 uid water production. This explains the agreement seen in previous sections until $t \approx$
 415 1130 LST, as all cases have the same domain-wide sensible heat flux and initial wind pro-

416 file. Perhaps the most interesting point to note is that in the 0% latent heat case any
 417 liquid water produced is solely from moisture that exists in the initial profile or that is
 418 introduced by the large-scale moisture flux forcing, both of which are applied uniformly
 419 in the domain. Still, the 0% latent heat case is able to produce liquid water at a rate ini-
 420 tially faster than the fully homogeneous case or any case considered in Sec. 3.2, and reaches
 421 a peak LWP value that is nearly equal to the fully homogeneous case. The importance
 422 of the spatial structure of the Bowen ratio, implied by the similarities in cloud produc-
 423 tion between the homogeneous, 0% latent heat, and 20% latent heat cases, is especially
 424 interesting in the context of Qin et al. (2018), who found that the Bowen ratio is a sig-
 425 nificant factor in land-atmosphere coupling, particularly in the Southwestern United States,
 426 in a study on the added value of superparameterizations to precipitation in global cli-
 427 mate models. These two results together continue to suggest that global ESMs could ben-
 428 efit from knowledge of SGS heterogeneity.

429 The liquid water production in the no wind case diverges from the heterogeneous
 430 and homogeneous cases just after 1030 LST and reaches a peak value larger than the base
 431 heterogeneous case approximately an hour earlier than the other cases. The TKE pro-
 432 duction in the no wind case begins development later than the heterogeneous and ho-
 433 mogeneous cases, but develops very quickly once production begins, reaching a peak value
 434 approximately two hours earlier than the heterogeneous and homogeneous cases, with
 435 a magnitude very similar to the homogeneous case. The w-e wind case follows the base
 436 heterogeneous case very closely in both liquid water and TKE production, but shows a
 437 larger peak value in both fields with a similar timing.

438 Maps of maximum LWP at each grid point throughout the simulation for the two
 439 modified wind cases are particularly informative (Fig. 13). The no wind case (Fig. 13a)
 440 produces very concentrated individual clouds of a spatial scale $\mathcal{O}(1 \text{ km})$ which themselves
 441 are very densely distributed in space (when considering the entire 15 hours together) over
 442 the entire dry portion of the domain, including the relatively small urban areas in the
 443 middle of the moist patch. The w-e wind case (Fig. 13b) shows a strong preference for
 444 liquid water production in the southern 30 km and northern 20 km of the domain, closely
 445 resembling the base heterogeneous case’s aversion to cloud production over the moist patch
 446 but realigned to the w-e wind direction. The general spatial pattern of cloud produc-
 447 tion occurring over drier areas of the land surface is very similar to those seen in a highly
 448 idealized study by Avissar and Liu (1996).

449 The no wind and w-e wind cases show a very visible preference for cloud develop-
 450 ment over the dry (and thus, warm) areas of the land surface compared to the moist (and
 451 cool) areas, and also add context to the pattern seen for the base heterogeneous case in
 452 Fig. 6a. The behavior of the modified wind cases largely supports the explanation of cir-
 453 culations driving liquid water development in the heterogeneous case, which appears to
 454 occur in the cross-stream direction when there is a prevailing wind. The no wind case,
 455 which reaches its peak LWP earlier and with a larger magnitude than the base hetero-
 456 geneous case, does lend some credence to the common wisdom that a mean wind will mix
 457 out surface heterogeneity. However, in addition to the differences between the base het-
 458 erogeneous and homogeneous cases, the w-e wind case shows a larger peak LWP than
 459 either the base heterogeneous case or the no wind case, indicating that there are yet-uncovered
 460 subtleties in the relationship between surface heterogeneity and the wind profile. We also
 461 see in the no wind case that, while previous results indicate that LWP and TKE do show
 462 some relation, a larger (smaller) amount of TKE does not immediately suggest a larger
 463 (smaller) cloud production. Finally, the exaggerated response to land-surface heterogene-
 464 ity seen in the no wind case eases potential concerns, to some degree, about the periodic
 465 lateral boundary conditions creating a positive feedback loop which amplifies the response
 466 of the atmosphere to heterogeneous surface fluxes.

3.4 Additional days

To justify the generality of the results seen here for September 24, 2017, two additional days at the SGP site are presented briefly for basic heterogeneous and homogeneous cases. These cases also use $\Delta_{x,y} = 100$ m, but are run on smaller $50 \text{ km} \times 50 \text{ km}$ domains. Analysis for these cases is limited to time series of LWP.

Time series of domain-averaged surface sensible heat and latent heat fluxes for the two days are shown in Fig. 14. Compared to September 24, 2017 where the majority of the surface energy is in the sensible heat flux, June 10, 2016 has similar magnitudes of surface sensible and latent heat flux (Fig. 14a) while July 16, 2017 has a majority of its surface energy in its latent heat flux (Fig. 14b). Maps of the surface sensible and latent heat flux at $t = 1238$ LST for the two days are shown in Fig. 15. Both days have land surfaces which are dominated by rainfall from previous days, but in different patterns from each other and from September 24, 2017. The June 10, 2016 case has a surface pattern where moist patches are present in the north-east and south-west corners of the domain (Fig. 15a1, b1), while the moist patch in the July 16, 2017 case dominates the eastern two-thirds of the domain (Fig. 15a2, b2).

The time series of domain-wide LWP for heterogeneous and homogeneous simulations of both days (Fig. 16) show even more extreme behavior than the September 24, 2017 simulations, where the heterogeneous cases produce significantly more overall liquid water than their respective homogeneous cases, and with different patterns in time. While analysis of these two additional days has been very brief, the effect of land-surface heterogeneity on domain-wide LWP for these cases is seen to be even more significant than for the September 24, 2017 case. This confirmation inspires confidence in the notion that land-surface heterogeneity produced by previous heavy rain events can have a large influence on cloud production in the right conditions.

4 Discussion

The initial explanation, arrived at largely visually, that emergent mesoscale circulations between coherent moist and dry patches in the land surface are responsible for the the differences between the heterogeneous and homogeneous cases in Sec. 3.1 appears to gain credibility in the subsequent experiments. It is seen in Sec. 3.2 that the large moist and dry patches are indeed responsible for the observed cloud production in the heterogeneous case. In Sec. 3.3 it is seen that, while larger sensible heat fluxes do enhance cloud production compared to the base homogeneous case, the increased cloud production in the heterogeneous case cannot be fully explained by the case's larger local sensible heat fluxes alone.

It can be seen in Fig. 11 that the two cases which are forced by the LSM which includes heterogeneous forcing meteorology (the heterogeneous and M cases) diverge from the other four cases in both their liquid water and TKE production at $t \approx 1130$ LST. If our proposition that this divergence in behaviors is caused by the onset of an emergent mesoscale circulation is correct, then we should expect to see no visible circulation pattern in the velocity fields of the heterogeneous case at $t \approx 1030$ LST, and subtle beginnings of the pattern seen in Fig. 7 at $t \approx 1230$ LST. To this end, Fig. 17 shows cross-sections of u in the x -direction for the heterogeneous case at $t = 1038$ LST and $t = 1238$ LST, i.e. just before and after the proposed triggering of mesoscale circulations. When $t = 1038$ LST, there is no visible circulation pattern in either the y -averaged u field (Fig. 17a) or in the individual cross-section of u taken at $y = 45$ km (Fig. 17b). At $t = 1238$ LST, however, the circulation pattern is clearly visible in both the y -averaged (Fig. 17c) and $y = 45$ km (Fig. 17d) cross-sections of u , with a band of strong positive u spanning from $x \approx 20$ km to $x \approx 80$ km at a height of $z \approx 4$ km with a corresponding band of strong negative u spanning the same range in x in the lower 2 km of the at-

517 mosphere. The velocity in the column between the two layers has become nearly qui-
 518 escent on average by 1238 LST and the beginnings of an emerging updraft can be seen
 519 at $x \approx 35$ km.

520 From the results seen here and in previous sections, it seems likely that both the
 521 magnitude and spatial scale of both land-surface and atmospheric heterogeneity, and the
 522 coupling between them, are important to understanding the dynamics of local cloud pro-
 523 duction, at least in certain cases. An interesting potential result is then that climate mod-
 524 els, which currently run on grids which are still largely $\mathcal{O}(100$ km), should not only in-
 525 clude considerations for SGS land-surface heterogeneity and mesoscale atmospheric cir-
 526 culations in their current cloud and turbulence parameterizations, but will find them-
 527 selves in a still challenging situation when grids get closer to $\mathcal{O}(10$ km), where the rel-
 528 evant scales of land-surface heterogeneity and the associated mesoscale circulations are
 529 similar to the grid scale, and thus cannot be fully resolved on the grid nor fully repre-
 530 sented in an SGS parameterization. This situation is reminiscent of the “gray zone” prob-
 531 lems seen in both the turbulence (Wyngaard, 2004) and cloud-modeling (Arakawa & Wu,
 532 2013) communities. As such, barring a meteoric leap in computing capabilities, it is pos-
 533 sible that representing land-surface heterogeneity will be an active and increasingly im-
 534 portant issue for climate models for the foreseeable future. While the study here focuses
 535 primarily on cloud production, the impact of land-surface heterogeneity on the overall
 536 Earth system is not isolated to convection. For example, it is suggested by Mendes and
 537 Prevedello (2020), based on analysis of satellite observations, that secondary circulations
 538 between patches of different vegetation types has a cooling effect on surface tempera-
 539 tures.

540 The LES experiments presented here are an initial investigation into the effects of
 541 realistic land-surface and atmospheric heterogeneity, and are intended to be built upon
 542 with the ultimate goal of providing useful numerical data for climate-scale diagnostic and
 543 parameterization development. The land-surface fields used to drive the LESs are from
 544 a diurnal cycle in a spun-up and fully functional LSM using real datasets for land cover,
 545 soil type, surface-routing terrain, and meteorology. The fields from the LSM are also as-
 546 similated with the observationally-improved VARANAL dataset, further ensuring real-
 547 istic energetics in the land surface. The spatial resolution and domain size are both also
 548 significant, with $\Delta_{x,y} = 100$ m over the 100 km \times 100 km domain and $\Delta_z = 30$ m in
 549 the lower 5 km of the vertical column. In this regard, the simulations conducted here
 550 offer a significant and novel increase in realism towards the study of the coupling between
 551 land and atmosphere heterogeneity in an ESM. However, there are still many idealiza-
 552 tions made in the simulations presented which warrant mentioning and examining fur-
 553 ther in future studies. The two most notable idealizations used here are: the semi-coupled
 554 LSM, where the land surface fields are specified *a priori* and do not receive feedback from
 555 the atmosphere as it is simulated, and, the periodic lateral boundary conditions.

556 The lack of a feedback between the atmosphere and the land surface means that
 557 clouds that develop do not influence the surface below. In particular, in these simula-
 558 tions clouds do not impact the local radiation budget of the land surface, which is one
 559 of the primary mechanisms of feedback from clouds to the land surface in the Earth sys-
 560 tem. The nature of coupling between clouds and surface radiation is generally a nega-
 561 tive feedback, where the presence of clouds reduces the radiation budget at the surface.
 562 Considering that the primary conclusion from the semi-coupled simulations here is that
 563 clouds develop over areas of high surface sensible heat flux, the inclusion of atmospheric
 564 feedback to the land surface could potentially have a large reductive impact on the re-
 565 sults seen here by reducing the local sensible heat flux once cloud production begins. Such
 566 a reduction could, in turn, have a damping effect on the generation of the mesoscale cir-
 567 culations observed here, which develop between dry and moist areas of the land surface.
 568 Future simulations which use a fully-coupled land surface, where the atmosphere can pro-
 569 vide online feedback to the LSM, are currently under development by the co-authors and

570 will provide valuable insights into both the model requirements for an LES with highly
 571 heterogeneous land-surface fields and the degree of feedback from atmospheric hetero-
 572 geneity to the land surface from a physical (though numerical) perspective.

573 The periodic lateral boundary conditions used in the simulations, while standard
 574 practice for LES and cloud-resolving studies, is another concession which potentially in-
 575 fluences the results seen here. The cloud production in the no wind case in Sec. 3.3 shows
 576 a significant temporal and spatial response to land-surface heterogeneity with a very vis-
 577 ible preference for production over drier areas of the land surface. It can thus be assumed
 578 that the observed results in the cases with wind are not reliant on the more numerical
 579 consequences of periodic lateral boundaries, for example the continual recycling of moist
 580 air across the domain. However, it is not clear how dependent the results are on the sus-
 581 tained fetches of high sensible heat adjacent to high latent heat that are created by the
 582 periodic boundaries. The $100 \text{ km} \times 100 \text{ km}$ domain used for the September 24, 2017 cases
 583 is large enough to fully encapsulate the moist patch in the land surface, but, while it is
 584 plausible to imagine, it cannot be assumed that similar patterns are repeated over the
 585 surrounding landscape. In conjunction with the fully-coupled simulations mentioned above,
 586 nested simulations are also being developed to investigate the influence of the periodic
 587 lateral boundary conditions used here.

588 It should also be mentioned that, while $\Delta_{x,y} = 100 \text{ m}$ is a very high resolution
 589 in the cloud-resolving arena, the horizontal resolution does present another potential source
 590 for improvement. Multiple idealized studies of the so-called gray zone as it relates to re-
 591 solving the ABL in an LES have found $\Delta_{x,y} = 100 \text{ m}$ to be a sufficient horizontal res-
 592 olution while $\Delta_{x,y} = 200 \text{ m}$ begins to show signs of grid-dependent turbulence devel-
 593 opment (e.g., Beare, 2014; Efsthathiou & Beare, 2015; J. S. Simon et al., 2019). By this
 594 standard, the resolution used here is near, but within, the limits of LES. It is not im-
 595 mediately clear how directly these and other idealized gray zone studies, which typically
 596 use uniform and constant surface sensible heat fluxes, translate to more realistic surface
 597 fluxes. In the simulations here, there is a small but noticeable burst of resolved TKE at
 598 $t \approx 0730 \text{ LST}$ in most of the cases (e.g., Fig. 5b), which is a common characteristic of
 599 an artificially delayed onset of resolved turbulence due to excessive horizontal dissipa-
 600 tion of momentum and diffusion of heat from the turbulence closure model. Such an ar-
 601 tifact in the early morning spin-up of the atmosphere does not necessarily indicate that
 602 the resolution is irredeemably coarse, so long as the delay of resolved turbulence is not
 603 significant and the overall dynamics are accurately simulated once turbulence is triggered.
 604 While the effect of the resolution seen here does not appear to be excessive, and the fields
 605 produced here certainly appear well-resolved, particularly the cross-sections of cloud mix-
 606 ing ratio in Figs. 7d and 8d, the effects of the horizontal resolution cannot fully be ap-
 607 preciated without comparison to even finer, as well as coarser, simulations of the same
 608 case. Such a study is currently under development and is anticipated to provide novel
 609 insights towards understanding land and atmosphere heterogeneity, as well as the gray
 610 zone of LES turbulence closure models in general.

611 Planned future work generally falls into one or both of two categories: clarifying
 612 the impact of different aspects of the LES configuration on cases with heterogeneous land
 613 surfaces, and, providing value to ongoing efforts towards diagnosing and modeling SGS
 614 heterogeneity in ESM parameterizations. On the clarification side, the aforementioned
 615 three studies (semi- vs. fully-coupled land surfaces, periodic vs. nested lateral bound-
 616 ary conditions, and an expanded range of horizontal resolutions) are the top priorities
 617 in the near future. Related to aiding diagnostic and parameterization efforts, the most
 618 immediate future work is focused on running heterogeneous and homogeneous simula-
 619 tions for multiple dozen additional days, with various initial conditions on the surface
 620 and in the atmosphere, at the SGP site aided by the available data from the LASSO cam-
 621 paign. In the longer term, we plan to extend simulations to additional locations around
 622 the globe where different forms of surface heterogeneity may be studied, e.g., lakes, moun-

tainous terrain, urban areas. These future studies are not exclusive efforts but will be conducted in conjunction with each other, i.e., model configuration choices will be tested for different days and locations, and knowledge gained regarding model behavior will be applied to the diagnostic and parameterization efforts when useful.

5 Summary and conclusions

Realistic land-surface fields are used to evaluate the role of land-surface heterogeneity on atmospheric dynamics by using high-resolution output from the HydroBlocks LSM to specify spatially heterogeneous and time-evolving surface conditions for sensible heat flux, latent heat flux, temperature (via emissivity and upward longwave radiation), albedo, and roughness coefficient in the WRF model, which is then run as a high-resolution LES over the SGP site in a variety of experiments. The primary experiment (Sec. 3.1) compares two simulations of the diurnal cycle on September 24, 2017: the first using the aforementioned heterogeneous surface fields and the second using time-evolving but spatially homogeneous surface fields, which take their uniform value of each field as the domain-average of the field in the heterogeneous case. It is observed that the heterogeneous case produces clouds more actively than the homogeneous case and in a spatial pattern that is correlated to the surface sensible heat flux fields. An explanation is offered that the heterogeneous simulation develops a circulation pattern between moist and dry areas where moist air originating over areas of high surface latent heat flux are transported laterally within the boundary layer to areas of high surface sensible heat flux, and are then lifted upwards through the boundary layer leading to cloud production.

Three sets of experiments which consider different modifications to the heterogeneous simulation are then presented, designed to elucidate the atmospheric dynamics generated by the heterogeneous land surface. The first set of modifications creates land surfaces which include only certain aspects of heterogeneity (Sec. 3.2). The second set of modifications increases the Bowen ratio in the heterogeneous case by converting local latent heat fluxes to sensible heat fluxes (Sec. 3.3). The final set of modifications uses the fully heterogeneous surfaces but adjusts the initial wind profile (Sec. 3.3). It is generally found that while there are many ways to produce more clouds and TKE than the fully homogeneous case, it is much more difficult to match the peak magnitude of cloud production seen in the heterogeneous case without the mesoscale patterns created in the surface heat fluxes by forcing the LSM with heterogeneous meteorology fields. The lack of similarity between cloud production in the base heterogeneous case and the cases with increased Bowen ratios shows that the areas with above-average sensible heat flux alone are not the source of the increased production, but that the remote latent heat fluxes are also necessary. We also see that re-orienting the prevailing wind in the atmosphere will correspondingly re-orient the cloud-production pattern to remain focused over the dry areas, and that removing the mean wind entirely allows clouds to form everywhere that is associated with a high surface sensible heat flux.

The last set of additional experiments is a brief analysis of two other summer days at the SGP site, both also with large, but unique, scales of spatial heterogeneity generated by scattered storms at the site on previous days (Sec. 3.4). Of the two additional days shown, the surface energy fluxes on June 10, 2016 are relatively evenly distributed between latent and sensible heat and the surface energy fluxes on July 16, 2017 are predominantly in the form of latent heat, providing complements to the primary September 24, 2017 case, where surface energy fluxes are predominantly in the form of sensible heat. Both additional days show a significantly larger domain-wide LWP values in the heterogeneous cases compared to their homogeneous counterparts.

Finally, a discussion of observations from the different experiments leads to further analysis and a bolstering of the mesoscale circulation explanation for the observed increase in cloud production seen in the heterogeneous case (Sec. 4). Potential shortcom-

674 ings of the simulations conducted for this study are also discussed, and future experi-
 675 ments are outlined. While the analysis presented here is largely for a single day there
 676 appears to be some generality to the conclusion that spatial heterogeneity of the land
 677 surface plays a key role in cloud production. It follows that SGS cloud and turbulence
 678 parameterizations for weather and climate models should also include information about
 679 SGS land-surface heterogeneity and vice versa, though an effective mechanism to do so
 680 is yet undeveloped. We hope that this and future work will aid in the development of
 681 such mechanisms.

682 Acknowledgments

683 Funded by NOAA grant NA19OAR4310241. PD's contribution is funded by NOAA grant
 684 NA19OAR4310242.

685 Data availability: Simulations here use a modification of WRF version 3.8.1 devel-
 686 oped and maintained by the LASSO team. The base WRF code, initial sounding files,
 687 and large-scale forcing files are available from W. Gustafson et al. (2019). Additional mod-
 688 ifications to the WRF code to specify heterogeneous surfaces, data files for surface fields
 689 for each simulation, and model control files for each simulation are available at J. Simon
 690 and Chaney (2021).

691 References

- 692 Albertson, J. D., Kustas, W. P., & Scanlon, T. M. (2001). Large-eddy simulation
 693 over heterogeneous terrain with remotely sensed land surface conditions. *Water*
 694 *Resources Research*, *37*(7), 1939–1953.
- 695 Arakawa, A., & Wu, C.-M. (2013). A unified representation of deep moist convection
 696 in numerical modeling of the atmosphere. Part I. *J. Atmos. Sci.*, *70*(7), 1977–
 697 1992. doi: 10.1175/JAS-D-12-0330.1
- 698 Avissar, R., & Liu, Y. (1996). Three-dimensional numerical study of shallow convective
 699 clouds and precipitation induced by land surface forcing. *Journal of Geo-*
 700 *physical Research: Atmospheres*, *101*(D3), 7499–7518.
- 701 Avissar, R., & Schmidt, T. (1998). An Evaluation of the Scale at which Ground-
 702 Surface Heat Flux Patchiness Affects the Convective Boundary Layer Using
 703 Large-Eddy Simulations. *Journal of the Atmospheric Sciences*, *55*(16), 2666-
 704 2689. Retrieved from [https://doi.org/10.1175/1520-0469\(1998\)055<2666:
 705 AEOTSA>2.0.CO;2](https://doi.org/10.1175/1520-0469(1998)055<2666:AEOTSA>2.0.CO;2) doi: 10.1175/1520-0469(1998)055(2666:AEOTSA)2.0.CO;
 706 2
- 707 Beare, R. J. (2014). A length scale defining partially-resolved boundary-layer turbu-
 708 lence simulations. *Boundary-Layer Meteorol.*, *151*(1), 39–55.
- 709 Bertoldi, G., Kustas, W. P., & Albertson, J. D. (2013). Evaluating source area
 710 contributions from aircraft flux measurements over heterogeneous land using
 711 large-eddy simulation. *Boundary-layer meteorology*, *147*(2), 261–279.
- 712 Bonan, G. B., Oleson, K. W., Vertenstein, M., Levis, S., Zeng, X., Dai, Y., . . . Yang,
 713 Z.-L. (2002). The land surface climatology of the Community Land Model
 714 coupled to the NCAR Community Climate Model. *Journal of climate*, *15*(22),
 715 3123–3149.
- 716 Bou-Zeid, E., Meneveau, C., & Parlange, M. B. (2004). Large-eddy simulation of
 717 neutral atmospheric boundary layer flow over heterogeneous surfaces: Blending
 718 height and effective surface roughness. *Water Resources Research*, *40*(2).
- 719 Chaney, N. W., Metcalfe, P., & Wood, E. F. (2016). HydroBlocks: a field-scale
 720 resolving land surface model for application over continental extents. *Hydro-*
 721 *logical Processes*, *30*(20), 3543-3559. Retrieved from [https://onlinelibrary
 722 .wiley.com/doi/abs/10.1002/hyp.10891](https://onlinelibrary.wiley.com/doi/abs/10.1002/hyp.10891) doi: 10.1002/hyp.10891
- 723 Chaney, N. W., Minasny, B., Herman, J. D., Nauman, T. W., Brungard, C. W.,
 724 Morgan, C. L., . . . Yimam, Y. (2019). POLARIS soil properties: 30-m prob-

- abilistic maps of soil properties over the contiguous United States. *Water Resources Research*, 55(4), 2916–2938.
- Chaney, N. W., Roundy, J. K., Herrera-Estrada, J. E., & Wood, E. F. (2015). High-resolution modeling of the spatial heterogeneity of soil moisture: Applications in network design. *Water Resources Research*, 51(1), 619–638.
- Chaney, N. W., Torres-Rojas, L., Vergopolan, N., & Fisher, C. K. (2020). Two-way coupling between the sub-grid land surface and river networks in Earth system models. *Geoscientific Model Development Discussions*, 2020, 1–31. Retrieved from <https://gmd.copernicus.org/preprints/gmd-2020-291/> doi: 10.5194/gmd-2020-291
- Chaney, N. W., Van Huijgevoort, M. H., Shevliakova, E., Malyshev, S., Milly, P. C., Gauthier, P. P., & Sulman, B. N. (2018). Harnessing big data to rethink land heterogeneity in Earth system models. *Hydrology and Earth System Sciences*, 22(6), 3311–3330.
- Chaney, N. W., Wood, E. F., McBratney, A. B., Hempel, J. W., Nauman, T. W., Brungard, C. W., & Odgers, N. P. (2016). POLARIS: A 30-meter probabilistic soil series map of the contiguous United States. *Geoderma*, 274, 54–67.
- Clark, M. P., Fan, Y., Lawrence, D. M., Adam, J. C., Bolster, D., Gochis, D. J., . . . others (2015). Improving the representation of hydrologic processes in Earth System Models. *Water Resources Research*, 51(8), 5929–5956.
- Cosgrove, B. A., Lohmann, D., Mitchell, K. E., Houser, P. R., Wood, E. F., Schaake, J. C., . . . others (2003). Real-time and retrospective forcing in the North American Land Data Assimilation System (NLDAS) project. *Journal of Geophysical Research: Atmospheres*, 108(D22).
- Ducharne, A., Koster, R. D., Suarez, M. J., Stieglitz, M., & Kumar, P. (2000). A catchment-based approach to modeling land surface processes in a general circulation model: 2. parameter estimation and model demonstration. *Journal of Geophysical Research: Atmospheres*, 105(D20), 24823–24838.
- Efstathiou, G., & Beare, R. J. (2015). Quantifying and improving sub-grid diffusion in the boundary-layer grey zone. *Q J R Meteorol Soc*, 141(693), 3006–3017.
- Findell, K. L., & Eltahir, E. A. (2003). Atmospheric controls on soil moisture-boundary layer interactions: Three-dimensional wind effects. *Journal of Geophysical Research: Atmospheres*, 108(D8).
- Golaz, J.-C., Larson, V. E., & Cotton, W. R. (2002). A PDF-based model for boundary layer clouds. Part I: Method and model description. *Journal of the atmospheric sciences*, 59(24), 3540–3551.
- Gómez-Plaza, A., Martínez-Mena, M., Albaladejo, J., & Castillo, V. (2001). Factors regulating spatial distribution of soil water content in small semiarid catchments. *Journal of hydrology*, 253(1-4), 211–226.
- Gustafson, W., Vogelmann, A., Cheng, X., Dumas, K., Endo, S., Johnson, K., . . . Xiao, H. (2019). Description of the LASSO data bundles product. DOE Atmospheric Radiation Measurement (ARM) user facility. *DOE/SC-ARM-TR-216*. doi: 10.2172/1469590
- Gustafson, W. I., Vogelmann, A. M., Li, Z., Cheng, X., Dumas, K. K., Endo, S., . . . Xiao, H. (2020). The Large-eddy simulation (LES) Atmospheric Radiation Measurement (ARM) Symbiotic Simulation and Observation (LASSO) activity for continental shallow convection. *Bulletin of the American Meteorological Society*, 101(4), E462–E479.
- Gutowski, W. J., Ullrich, P. A., Hall, A., Leung, L. R., O'Brien, T. A., Patricola, C. M., . . . others (2020). The ongoing need for high-resolution regional climate models: Process understanding and stakeholder information. *Bulletin of the American Meteorological Society*, 101(5), E664–E683.
- Han, C., Brdar, S., Raasch, S., & Kollet, S. (2019). Large-eddy simulation of catchment-scale circulation. *Quarterly Journal of the Royal Meteorological Society*, 145(720), 1218–1233.

- 780 Homer, C. H., Fry, J. A., & Barnes, C. A. (2012). The national land cover database.
781 *US Geological Survey Fact Sheet, 3020*(4), 1–4.
- 782 Huang, H.-Y., & Margulis, S. A. (2013). Impact of soil moisture heterogeneity
783 length scale and gradients on daytime coupled land-cloudy boundary layer
784 interactions. *Hydrological Processes, 27*(14), 1988–2003.
- 785 Jacobs, J., Mohanty, B., Hsu, E., & Miller, D. (2004). Field scale variability and
786 similarity of soil moisture. *Remote Sens. Environ, 92*, 436–446.
- 787 Kang, S.-L. (2016). Regional Bowen ratio controls on afternoon moist convection: A
788 large eddy simulation study. *Journal of Geophysical Research: Atmospheres,*
789 *121*(23), 14,056–14,083. Retrieved from [https://agupubs.onlinelibrary](https://agupubs.onlinelibrary.wiley.com/doi/abs/10.1002/2016JD025567)
790 [.wiley.com/doi/abs/10.1002/2016JD025567](https://agupubs.onlinelibrary.wiley.com/doi/abs/10.1002/2016JD025567) doi: 10.1002/2016JD025567
- 791 Kang, S.-L. (2020). Effects of mesoscale surface heterogeneity on the afternoon and
792 early evening transition of the atmospheric boundary layer. *Boundary-Layer*
793 *Meteorology, 174*(3), 371–391.
- 794 Kustas, W. P., & Albertson, J. D. (2003). Effects of surface temperature contrast on
795 land-atmosphere exchange: A case study from monsoon 90. *Water Resources*
796 *Research, 39*(6).
- 797 Lawrence, D. M., Fisher, R. A., Koven, C. D., Oleson, K. W., Swenson, S. C., Bo-
798 nan, G., ... others (2019). The Community Land Model version 5: Description
799 of new features, benchmarking, and impact of forcing uncertainty. *Journal of*
800 *Advances in Modeling Earth Systems, 11*(12), 4245–4287.
- 801 Lin, Y., & Mitchell, K. E. (2005). The NCEP stage II/IV hourly precipitation anal-
802 yses: Development and applications. In *Proceedings of the 19th conference hy-*
803 *drology, american meteorological society, san diego, ca, usa* (Vol. 10).
- 804 Mendes, C. B., & Prevedello, J. A. (2020). Does habitat fragmentation affect
805 landscape-level temperatures? A global analysis. *Landscape Ecology, 35*(8),
806 1743–1756.
- 807 Milly, P. C., Malyshev, S. L., Shevliakova, E., Dunne, K. A., Findell, K. L., Gleeson,
808 T., ... Swenson, S. (2014). An enhanced model of land water and energy
809 for global hydrologic and earth-system studies. *Journal of Hydrometeorology,*
810 *15*(5), 1739–1761.
- 811 Mitchell, K. E., Lohmann, D., Houser, P. R., Wood, E. F., Schaake, J. C., Robock,
812 A., ... others (2004). The multi-institution North American Land Data As-
813 similation System (NLDAS): Utilizing multiple GCIP products and partners in
814 a continental distributed hydrological modeling system. *Journal of Geophysical*
815 *Research: Atmospheres, 109*(D7).
- 816 Niu, G.-Y., Yang, Z.-L., Mitchell, K. E., Chen, F., Ek, M. B., Barlage, M., ... oth-
817 ers (2011). The community Noah land surface model with multiparameteriza-
818 tion options (Noah-MP): 1. model description and evaluation with local-scale
819 measurements. *Journal of Geophysical Research: Atmospheres, 116*(D12).
- 820 Ntelekos, A. A., Smith, J. A., Baeck, M. L., Krajewski, W. F., Miller, A. J., &
821 Goska, R. (2008). Extreme hydrometeorological events and the urban en-
822 vironment: Dissecting the 7 July 2004 thunderstorm over the Baltimore MD
823 Metropolitan Region. *Water Resources Research, 44*(8).
- 824 Phillips, T. J., & Klein, S. A. (2014). Land-atmosphere coupling manifested in
825 warm-season observations on the US southern great plains. *Journal of Geo-*
826 *physical Research: Atmospheres, 119*(2), 509–528.
- 827 Pielke Sr, R. A. (2001). Influence of the spatial distribution of vegetation and soils
828 on the prediction of cumulus convective rainfall. *Reviews of Geophysics, 39*(2),
829 151–177.
- 830 Qin, H., Pritchard, M. S., Kooperman, G. J., & Parishani, H. (2018). Global ef-
831 fects of superparameterization on hydrothermal land-atmosphere coupling on
832 multiple timescales. *Journal of Advances in Modeling Earth Systems, 10*(2),
833 530–549.
- 834 Senatore, A., Mendicino, G., Gochis, D. J., Yu, W., Yates, D. N., & Kunstmann,

- 835 H. (2015). Fully coupled atmosphere-hydrology simulations for the central
 836 Mediterranean: Impact of enhanced hydrological parameterization for short
 837 and long time scales. *Journal of Advances in Modeling Earth Systems*, 7(4),
 838 1693–1715.
- 839 Sengupta, M., Clothiaux, E. E., Ackerman, T. P., Kato, S., & Min, Q. (2003).
 840 Importance of accurate liquid water path for estimation of solar radiation in
 841 warm boundary layer clouds: An observational study. *Journal of climate*,
 842 16(18), 2997–3009.
- 843 Shao, Y., Liu, S., Schween, J. H., & Crewell, S. (2013). Large-eddy atmosphere-
 844 land-surface modelling over heterogeneous surfaces: Model development and
 845 comparison with measurements. *Boundary-layer meteorology*, 148(2), 333–
 846 356.
- 847 Shrestha, P., Sulis, M., Masbou, M., Kollet, S., & Simmer, C. (2014). A scale-
 848 consistent terrestrial systems modeling platform based on COSMO, CLM, and
 849 ParFlow. *Monthly weather review*, 142(9), 3466–3483.
- 850 Simon, J., & Chaney, N. (2021, May). *Data for: Semi-coupling of a Field-scale*
 851 *Resolving Land-surface Model and WRF-LES to Investigate the Influence of*
 852 *Land-surface Heterogeneity on Cloud Development*. Zenodo. Retrieved from
 853 <https://doi.org/10.5281/zenodo.4741327> doi: 10.5281/zenodo.4741327
- 854 Simon, J. S., Zhou, B., Mirocha, J. D., & Chow, F. K. (2019). Explicit filtering
 855 and reconstruction to reduce grid dependence in convective boundary layer
 856 simulations using WRF-LES. *Mon Weather Rev*, 147(5), 1805–1821. doi:
 857 10.1175/MWR-D-18-0205.1
- 858 Skamarock, W., Klemp, J., Dudhia, J., Gill, D., Barker, D., Duda, M., . . . Powers,
 859 J. (2008). A description of the Advanced Research WRF version 3. *NCAR*
 860 *Technical Note, NCAR/TN-475+STR*.
- 861 Sušelj, K., Teixeira, J., & Chung, D. (2013). A unified model for moist convective
 862 boundary layers based on a stochastic eddy-diffusivity/mass-flux parameteriza-
 863 tion. *Journal of the Atmospheric Sciences*, 70(7), 1929–1953.
- 864 Talbot, C., Bou-Zeid, E., & Smith, J. (2012). Nested mesoscale large-eddy simula-
 865 tions with WRF: Performance in real test cases. *Journal of Hydrometeorology*,
 866 13(5), 1421–1441.
- 867 Taylor, C. M., de Jeu, R. A., Guichard, F., Harris, P. P., & Dorigo, W. A. (2012).
 868 Afternoon rain more likely over drier soils. *Nature*, 489(7416), 423–426.
- 869 Taylor, C. M., Gounou, A., Guichard, F., Harris, P. P., Ellis, R. J., Couvreur, F., &
 870 De Kauwe, M. (2011). Frequency of Sahelian storm initiation enhanced over
 871 mesoscale soil-moisture patterns. *Nature Geoscience*, 4(7), 430–433.
- 872 Timmermans, W., Bertoldi, G., Albertson, J., Olioso, A., Su, Z., & Gieske, A.
 873 (2008). Accounting for atmospheric boundary layer variability on flux estima-
 874 tion from rs observations. *International journal of remote sensing*, 29(17-18),
 875 5275–5290.
- 876 Vergopolan, N., Chaney, N. W., Beck, H. E., Pan, M., Sheffield, J., Chan, S., &
 877 Wood, E. F. (2020). Combining hyper-resolution land surface modeling with
 878 SMAP brightness temperatures to obtain 30-m soil moisture estimates. *Remote*
 879 *Sensing of Environment*, 242, 111740.
- 880 Western, A. W., Grayson, R. B., Blöschl, G., Willgoose, G. R., & McMahon, T. A.
 881 (1999). Observed spatial organization of soil moisture and its relation to
 882 terrain indices. *Water resources research*, 35(3), 797–810.
- 883 Wyngaard, J. C. (2004). Toward numerical modeling in the “terra incognita”.
 884 *J. Atmos. Sci.*, 61(14), 1816–1826. doi: 10.1175/1520-0469(2004)061<1816:
 885 TNMITT>2.0.CO;2

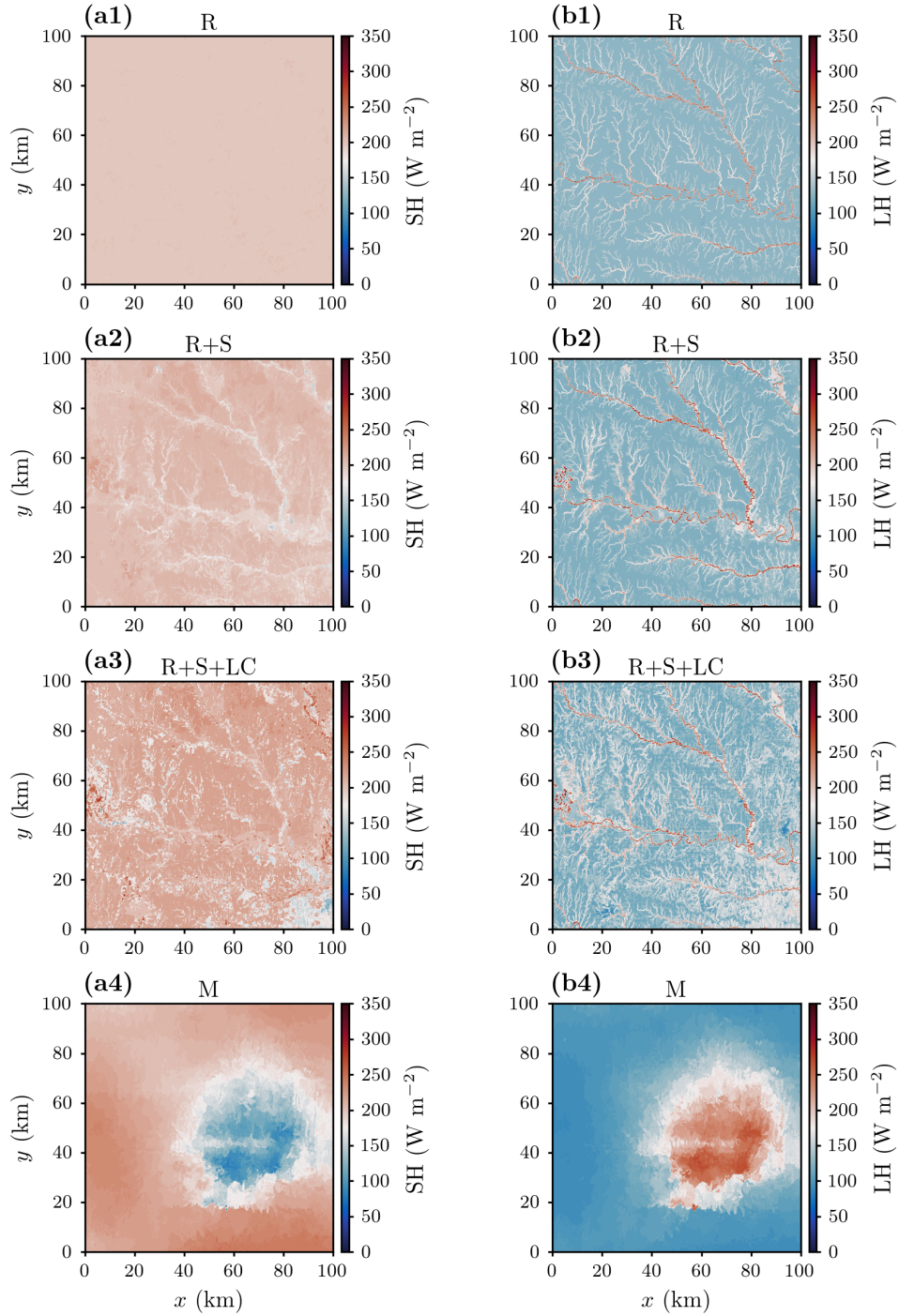


Figure 10. (column a) Surface sensible heat flux and (column b) latent heat flux fields for September 24, 2017 simulations at $t = 1238$ LST with land surfaces which include heterogeneity from: (row 1) only rivers (R), (row 2) rivers and soil type (R+S), (row 3) rivers, soil type and land cover (R+S+LC), and (row 4) only forcing meteorology (M).

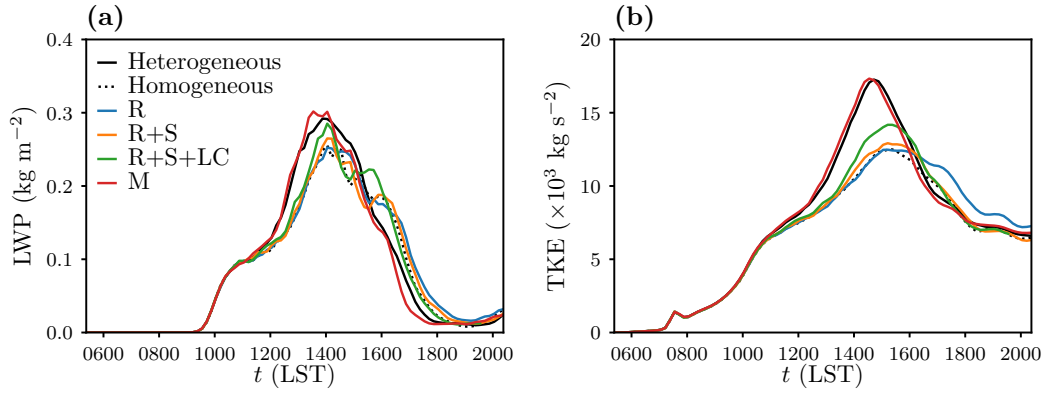


Figure 11. Domain-wide fields in time from the September 24, 2017 simulations where the land model includes heterogeneity from only rivers (R), rivers and soil type (R+S), rivers, soil type and land cover (R+S+LC), and only forcing meteorology (M): (a) LWP, (b) vertically integrated, mass-coupled TKE. The fully heterogeneous and fully homogeneous cases are also shown for comparison.

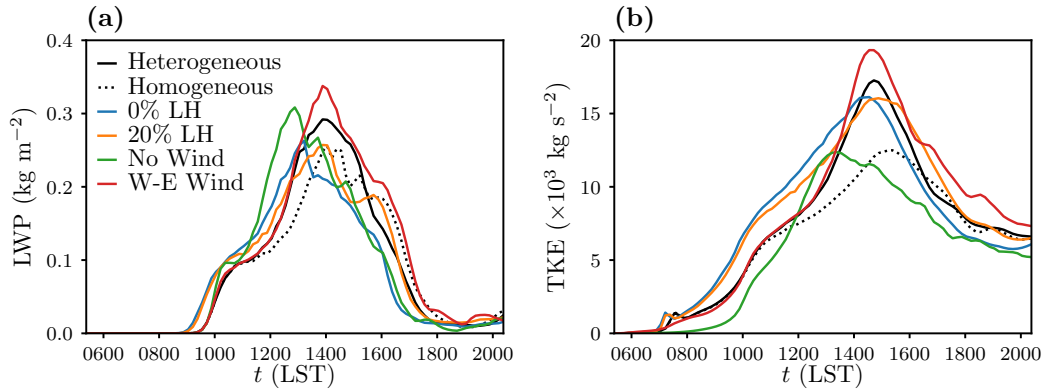


Figure 12. Domain-wide fields in time from the 0% LH, 20% LH, no wind, and w-e wind simulations of September 24, 2017: (a) LWP, (b) vertically integrated, mass-coupled TKE. The fully heterogeneous and fully homogeneous cases are also shown for comparison.

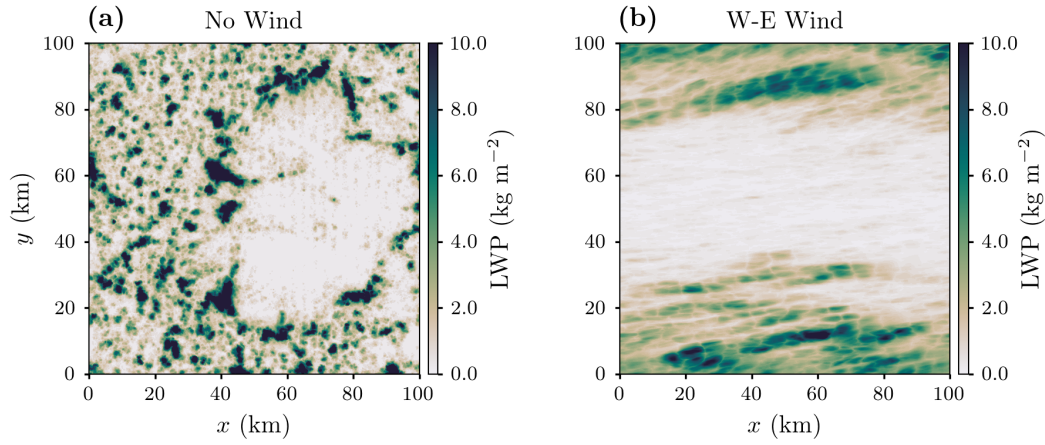


Figure 13. Maximum values of LWP at each grid point throughout the duration of September 24, 2017 simulations with different initial wind profiles: (a) modified to have zero initial mean wind in the column and (b) re-oriented to a purely west-east initial mean wind.

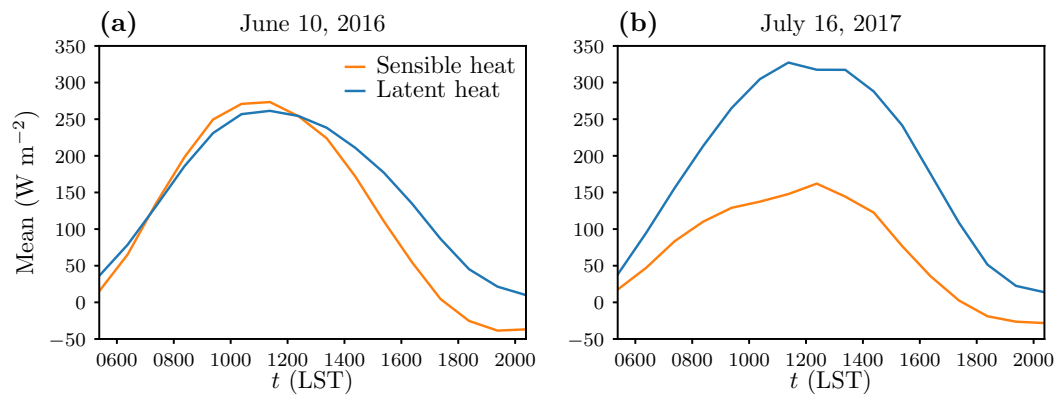


Figure 14. Time series of the domain mean surface sensible heat and latent heat fluxes used for simulations of: (a) June 10, 2016 and (b) July 16, 2017.

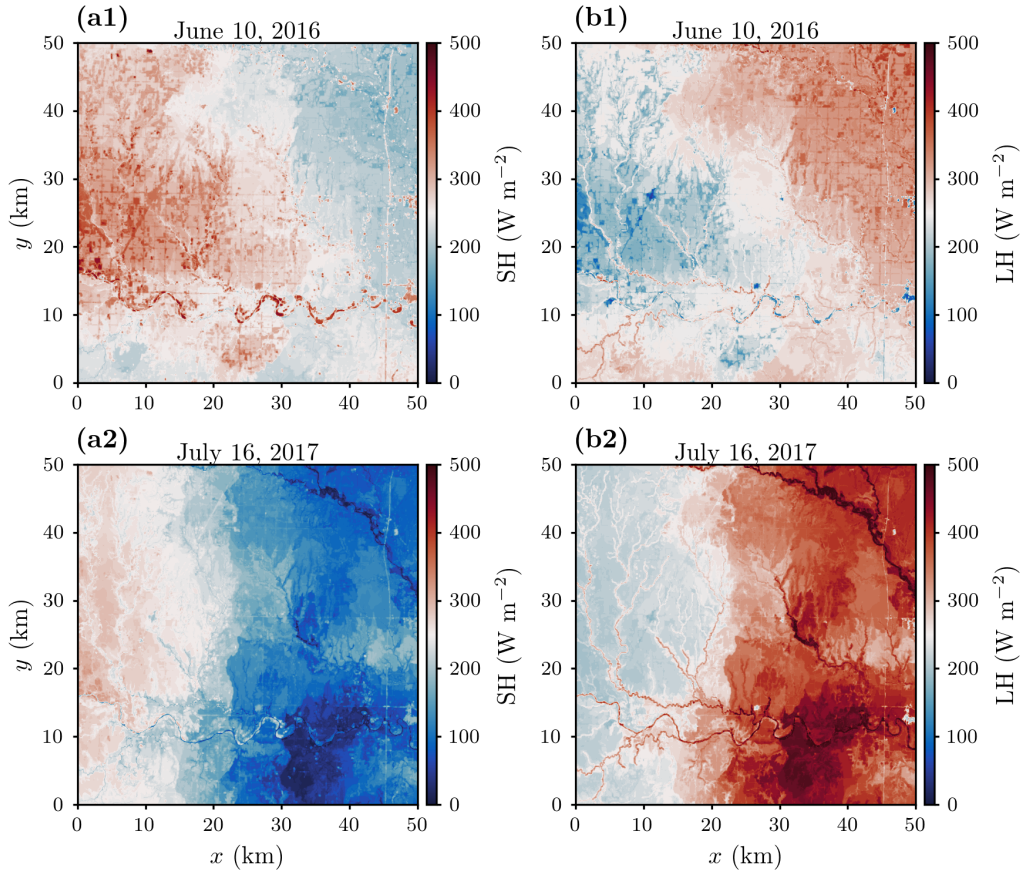


Figure 15. (column a) Surface sensible heat flux and (column b) latent heat flux fields at $t = 1238$ LST for simulations of: (row 1) June 10, 2016 and (row 2) July 16, 2017.

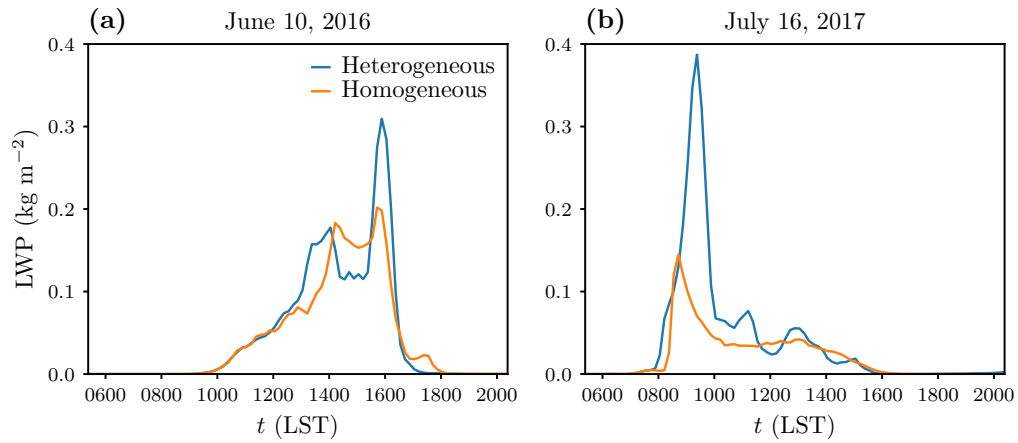


Figure 16. Domain-wide LWP in time from the heterogeneous and homogeneous simulations of: (a) June 10, 2016 and (b) July 16, 2017.

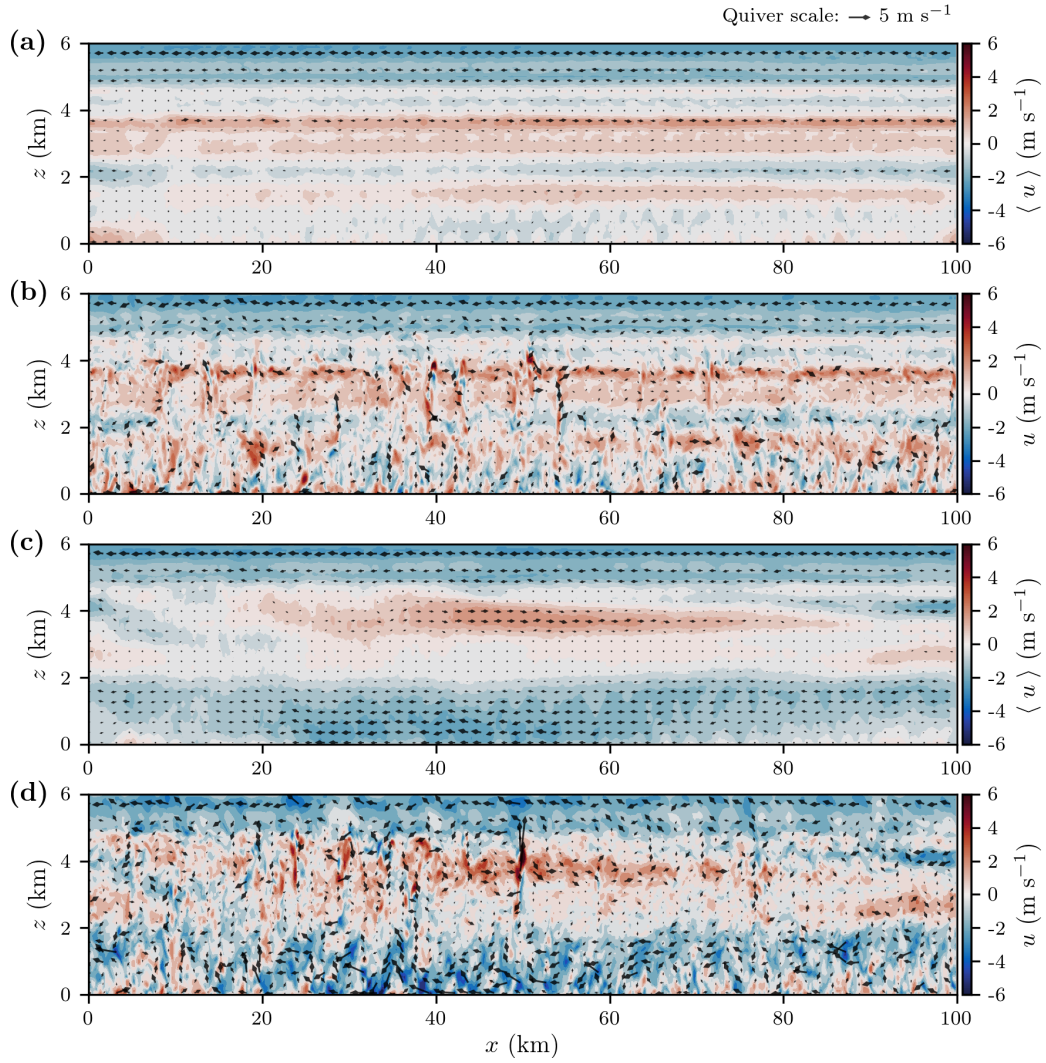


Figure 17. Profiles from the September 24, 2017 simulation using heterogeneous surfaces (from Sec. 3.1) of: (a) u -velocity along x and domain-averaged in y at $t = 1038$ LST, (b) u -velocity along x at $y = 45$ km and $t = 1038$ LST, (c) u -velocity along x and domain-averaged in y at $t = 1238$ LST, (d) u -velocity along x at $y = 45$ km and $t = 1238$ LST.